

# Ozone formation sensitivity based on the secondary formaldehyde-to-nitrogen dioxide ratio (FNR<sub>sec</sub>) derived from ground-based remote sensing measurements and a chemical transport model

Nguyen Doan Thien Chi<sup>1,2</sup>, Hiroshi Tanimoto<sup>1,2</sup>, Satoshi Inomata<sup>2</sup>, Kohei Ikeda<sup>2</sup>, Yange Deng<sup>2</sup>, Royston Uning<sup>2</sup>, Tamaki Fujinawa<sup>2</sup>, Astrid Müller<sup>2</sup>, Masatomo Fujiwara<sup>3</sup>, Shungo Kato<sup>4</sup>, Hisahiro Takashima<sup>5</sup>

<sup>1</sup> Graduate School of Environmental Studies, Nagoya University, Furo-cho, Chikusa-ku, Nagoya 464-8601, Japan

<sup>2</sup> National Institute for Environmental Studies, 16-2 Onogawa, Tsukuba, Ibaraki 305-8506, Japan

<sup>3</sup> Faculty of Environmental Earth Science, Hokkaido University, Sapporo 060-0810, Japan

<sup>4</sup> Faculty of Urban Environmental Sciences, Tokyo Metropolitan University, 1-1 Minami-Osawa, Hachioji, Tokyo 192-0397, Japan

<sup>5</sup> Faculty of Science, Fukuoka University, 8-19-1 Nanakuma, Jonan-ku, Fukuoka 814-0180, Japan

*Correspondence to:* Nguyen Doan Thien Chi (nguyen.doanhtienchi@nies.go.jp) and Hiroshi Tanimoto (tanimoto@nies.go.jp)

**Abstract.** Sensitivity analysis is essential for developing effective ozone (O<sub>3</sub>) mitigation strategies. This study aims to extensively investigate the diurnal, seasonal, and vertical chemical sensitivity of O<sub>3</sub> using a photochemical indicator, the secondary formaldehyde (HCHO)-to-nitrogen dioxide (NO<sub>2</sub>) ratio (FNR<sub>sec</sub>) as measured by Pandora remote-sensing spectrometers located across Japan. Region-specific FNR<sub>sec</sub> thresholds were determined using the GEOS-Chem chemical transport model. Surface concentrations and vertical column amounts of HCHO and NO<sub>2</sub> were obtained from in situ measurements and Pandora spectrometers. The concentrations of HCHO and NO<sub>2</sub> varied with season and altitude. Moreover, external pollution transport affected the vertical profiles and likely contributed to elevated concentrations. During exceedance events, the O<sub>3</sub> sensitivity analysis showed that NO<sub>x</sub>-limited conditions were dominant in summer, transitional regimes in spring and fall. Vertically, RO<sub>x</sub>-limited conditions typically formed near the surface layers, followed by transitional regimes in the mid-levels, and NO<sub>x</sub>-limited regimes aloft. Therefore, O<sub>3</sub> mitigation strategies should target not only the surface level but also elevated altitudes. This study contributes to fostering a comprehensive understanding of O<sub>3</sub> sensitivity in the troposphere using FNR<sub>sec</sub> retrieved from Pandora measurements.

**Keywords:** ozone chemical regime, Pandora, FNR<sub>sec</sub>, GEOS-Chem model.

## 1. Introduction

Tropospheric ozone (O<sub>3</sub>) is a central secondary pollutant formed through photochemical reactions involving its main precursors: nitrogen oxides (NO<sub>x</sub>, including NO and NO<sub>2</sub>) and volatile organic compounds (VOCs) in the presence of sunlight. Increases in tropospheric O<sub>3</sub> levels negatively affect human health (Liu et al., 2018; Nuvolone et al., 2018), crop productivity (Mahmood et al., 2020; Ramya et al., 2023), and ecosystems (Feng et al., 2021; Grulke and Heath, 2020). Due to its well-known impacts, enormous efforts have been made in many cities and countries to mitigate O<sub>3</sub> pollution (Hu et al., 2024; Chang et al., 2025; Shi et al., 2025a). A major challenge that hinders O<sub>3</sub> pollution mitigation strategy is that O<sub>3</sub> formation results from non-linear photochemical reactions of its precursors, rather than from direct emissions (Mishra et al., 2024; Sadanaga et al., 2017). Internally, O<sub>3</sub> production is initiated by the formation of peroxy radical (RO<sub>x</sub>), generated through reactions between VOCs and hydroxyl radical (OH). O<sub>3</sub> is subsequently produced when RO<sub>x</sub> radicals (HO<sub>2</sub> or RO<sub>2</sub>) react with NO, leading to radical propagation (Kleinman et al., 2001; Sillman and He, 2002). The radical termination proceeds control the O<sub>3</sub> production. These proceeds occur either through the reaction of OH with NO<sub>x</sub> to form nitric acid (referred as LNO<sub>x</sub>) or through radical-radical reactions (referred as LRO<sub>x</sub>) (Schroeder et al., 2017).

Sensitivity analysis is of significant importance for developing effective O<sub>3</sub> mitigation strategies. Tropospheric O<sub>3</sub> production is conventionally categorized into three regimes: NO<sub>x</sub>-limited (or NO<sub>x</sub>-sensitive) regime, transitional regime, and

radical-limited (also referred to as VOC-limited, VOC-sensitive, or NO<sub>x</sub>-saturated) regime. Depending on the sensitivity regime, controlling either NO<sub>x</sub> or VOC emissions can be an effective approach to mitigating O<sub>3</sub> pollution. Sensitivity analyses have been conducted using various approaches, including model-based methods (Thorp et al., 2021), absolute sensitivity analysis (Sakamoto et al., 2019), and photochemical indicators such as the formaldehyde-to-nitrogen dioxide ratio (FNR) (Jung et al., 2022; Qian et al., 2024; Souri et al., 2023b), the robust H<sub>2</sub>O<sub>2</sub>-to-HNO<sub>3</sub> ratio (Hammer, et al., 2002; Souri et al., 2023a), and the LRO<sub>x</sub>/LNO<sub>x</sub> ratio (Abdi-Oskouei et al., 2022; Schroeder et al., 2017). O<sub>3</sub> formation sensitivity can be visually represented using empirical kinetics modeling approach (EKMA) that produces curves between NO<sub>x</sub> and VOCs (Tonnesen and Dennis, 2000). However, measuring hundreds of VOC species is impractical. Meanwhile, HCHO reflects the VOC oxidation strength and is widely used as a proxy for VOCs reactivity (Irie et al., 2021). It should be noted that only secondary HCHO, produced photochemically from VOCs, accurately reflects the VOC oxidation capacity (Xue et al., 2022). Primary HCHO is directly emitted from anthropogenic activities; therefore, considering primary HCHO may be misleading in the assessment of VOCs reactivity. Previously, the HCHO-to-NO<sub>y</sub> ratio was used as an indicator of the chemical sensitivity. NO<sub>y</sub> consists of NO<sub>x</sub> and NO<sub>z</sub> (including HNO<sub>3</sub>, HONO, organic nitrates, etc.). The HCHO-to-NO<sub>2</sub> ratio has been proposed as a better indicator because HCHO and NO<sub>2</sub> have similar lifetimes and better represent the competition for OH radicals (Santiago et al., 2021; Tonnesen and Dennis, 2000). The FNR has inherent limitations in representing O<sub>3</sub> chemistry (Souri et al., 2023a). A wide transition/ambiguous range of FNR values has been reported compared with the more precise LNO<sub>x</sub>/LRO<sub>x</sub> ratio (Schroeder et al., 2017). Consequently, under certain conditions, FNR may misclassify O<sub>3</sub> formation sensitivity. Nonetheless, FNR remains a commonly used indicator because it can be readily obtained and does not require extensive modeling.

O<sub>3</sub> formation occurs not only at the surface but also at elevated altitudes in the troposphere (Hu et al., 2024). Moreover, due to atmospheric convection, elevated O<sub>3</sub> can be dispersed downward to the near-surface layer (Souri et al., 2021). Indeed, study of O<sub>3</sub> production within the planetary boundary layer (PBL) is more important than at the surface alone. VOCs, such as isoprene emitted from vegetation, can be vertically transported to higher layer, where they produce RO<sub>x</sub> radicals and secondarily formed HCHO through photochemical processes. The vertical distributions of HCHO is therefore primarily driven by vertical transport and chemistry, which complicates the vertical formation of tropospheric O<sub>3</sub> (Souri et al., 2023b). To investigate the vertical sensitivity of O<sub>3</sub> formation, previous studies have employed column FNR observed by multi-axis differential optical absorption spectroscopy (MAX-DOAS) (Irie et al., 2021; Zhang et al., 2021; Ryan et al., 2023; Wang et al., 2025). Other studies have applied satellite-based techniques to assess the spatial sensitivity of O<sub>3</sub> formation (Duncan et al., 2010; Jin et al., 2017; Jung et al., 2022). By combining satellite and ground-based remote sensing, column FNR sheds light on the development of spatially and temporally targeted O<sub>3</sub> mitigation strategies.

The Pandora instrument is a passive UV-VIS spectrometer that observes solar photons over the 280–530 nm spectral range (Herman et al., 2009). The Pandonia Global Network (PGN) is a joint project supported by NASA and ESA, providing real-time, standardized, calibrated, and verified air quality data along with associated uncertainty estimates (<https://www.pandonia-global-network.org/>). With more than 200 operational stations worldwide, the PGN has been widely applied in atmospheric research. In particular, due to their high accuracy, Pandora instruments have served as Fiducial Reference Measurement (FRM) for validating satellite observations (Douros et al., 2023; Judd et al., 2020; Kim et al., 2023) and airborne spectrometers (Choo et al., 2023; Judd et al., 2019). Additionally, Pandora observations have successfully highlighted the seasonal and diurnal variations of air pollutants (Herman and Mao, 2024; Liu et al., 2024). Mouat et al. (2024) reported a complex, heterogeneous environment near an airport using Pandora data. With its two viewing geometries, namely direct-sun and sky-scan modes, Pandora quantitatively observes total column amounts and lower tropospheric column amounts of several trace gases, including NO<sub>2</sub>, HCHO, and SO<sub>2</sub> (Cede et al., 2021a, b). Furthermore, the instrument provides both column and vertical distribution information, making it appropriate for investigating the O<sub>3</sub> formation sensitivity. Nevertheless, no studies have employed Pandora to analyze O<sub>3</sub> formation sensitivity.

Increased levels of air pollution not only influence health but also place a burden on socioeconomic costs and healthcare resources (Xu et al., 2025). Japan is facing the problem of an aging population that is more vulnerable to air pollution. A modeling study predicted that 80 % of Japan's population could be exposed to the highest levels of O<sub>3</sub> between 2030 and 2050 if no climate change mitigation policies are implemented (Chen et al., 2024). Looking back on history, the first episode of photochemical air pollution occurred in 1970, leading to the hospitalization of schoolchildren and high school students (Akimoto, 2017). In response, the government has implemented stringent emission controls since the 1980s, leading to a 56 % reduction in NO<sub>x</sub> and a 50 % reduction in VOCs emissions from 2000 to 2019 (Chatani et al., 2023). Despite the emission reductions, O<sub>3</sub> level remain unpredictable due to non-linear photochemical processes and an increase in transboundary transport (Akimoto, 2017; Irie et al., 2021). Therefore, extensive studies on O<sub>3</sub> formation are needed to more efficiently mitigate human exposure.

In this study, we first utilized both Pandora direct-sun and sky-scan modes to analyze O<sub>3</sub> formation sensitivity at different altitudes and latitudes across Japan. The Japan Pandora Network (JPN), as part of the PGN, has established more than 10 stations, providing real-time vertical measurements. Because FNR threshold values depend on the study region, meteorological conditions, and emissions, we applied the GEOS-Chem chemical transport model to determine region-specific FNR thresholds for Japan. To improve accuracy, we accounted for secondary HCHO contributions. The findings of this study provide scientific insights into the application of Pandora measurements for mitigating regional O<sub>3</sub> pollution.

## 2. Methodology

### 2.1 Surface measurements

To obtain surface concentrations of HCHO and NO<sub>2</sub>, we conducted in situ measurements at Tokyo Metropolitan University (Tokyo-TMU) during the summer (July 1–19) and fall (October 17–31) of 2022. NO<sub>2</sub> was measured using a cavity attenuated phase shift (CAPS) analyzer, which directly detects NO<sub>2</sub> by measuring absorption around 450 nm, with a detection limit of less than 0.1 ppb (Choi et al., 2020). Meanwhile, HCHO was obtained using a selected ion flow tube mass spectrometer (SIFT-MS). SIFT-MS utilizes precursor ions such as H<sub>3</sub>O<sup>+</sup>, NO<sup>+</sup>, and O<sub>2</sub><sup>+</sup> for ionization and detection of target substances (Langford et al., 2023; Roberts et al., 2022). This instrument is recommended as an efficient method for the measurement of HCHO in both indoor and outdoor environments (Zogka et al., 2022).

Surface O<sub>3</sub> concentrations were obtained from nearby air monitoring stations using the UV absorption method. These stations are operated by the Atmospheric Environmental Regional Observation System (AEROS) (<https://soramame.env.go.jp/>).

### 2.2 Tropospheric column amounts and vertical profiles derived from Pandora observations

Pandora spectrometer consists of a head sensor, an optical fiber transmission system, and a charge-coupled device (CCD) used as a spectral detector. The data retrieval begins with the raw measurement spectra (L0). The corrected signal (L1) is obtained by applying complex corrections, such as dark correction, latency correction, etc. Spectral fitting (L2Fit) is performed to derive slant column densities relative to a reference spectrum using the differential optical absorption spectroscopy (DOAS) method. Finally, L2 data is produced by converting slant columns into vertical columns utilizing geometrical air mass factors (AMFs) for the direct-sun mode and analytical methods for the sky-scan mode (Rawat et al., 2025). The direct-sun mode measures total NO<sub>2</sub> column with high precision ( $2.7 \times 10^{14}$  molecules cm<sup>-2</sup>) and accuracy ( $2.7 \times 10^{15}$  molecules cm<sup>-2</sup>). For total HCHO column, a statistical error of 6 % and a systematic error of 26 % have been reported (Spinei et al., 2018). The bias of the sky-scan measurement is approximately  $-0.02 \times 10^{16}$  molecules cm<sup>-2</sup> for NO<sub>2</sub> and  $-0.05 \times 10^{16}$  molecules cm<sup>-2</sup> for HCHO (Tirpitz et al., 2021; Verhoelst et al., 2021). In this study, we explored both the tropospheric column FNR and vertical FNR profile by combining the direct-sun and sky-scan modes of Pandora. In the direct-sun mode, the tropospheric columns of NO<sub>2</sub> and HCHO

were derived by subtracting the stratospheric contribution. This stratospheric information was derived from the GEOS-Chem model (Sect. 2.3). In addition to column densities in the lower troposphere (up to an altitude of 3 km), the sky-scan measurements provided vertical distributions from the surface up to an altitude of 3 km with several layers of measurements. These profiles are crucial for examining the vertical characteristics of NO<sub>2</sub> and HCHO, as well as O<sub>3</sub> production in the troposphere.

We used the Pandora data at four JPN stations, Sapporo, Tsukuba-NIES, Tokyo-TMU, and Fukuoka. These stations, listed from north to south, were chosen to investigate FNR across different latitude environments. A brief description of these Pandora stations is provided in Table S1 of the Supplementary Information. These Pandora instruments routinely alternate between direct-sun and sky-scan modes on a standard schedule (Cede et al., 2021a). Data processing was performed using the Blick software, which converts L0 (raw measurement spectra) to L2 products (e.g., vertical column densities, profiles, etc.). For FNR calculations, L2 products were employed. To maximize the available scientific data, we applied a new filtering method adopted from Rawat et al. (2025). The cut-off values were defined as the mean plus three standard deviations of the independence uncertainty for data with a high-quality flag. Data with independence uncertainty exceeding the cut-off value was removed. We also excluded data with a solar zenith angle (SZA) > 75° (Mouat et al., 2024). Using this filtering method, the data volume increased significantly by 5–30 % for NO<sub>2</sub> and 20–70 % for HCHO, compared to the filtering method that uses high and medium data quality flags.

### 2.3 Model simulations and determination of FNR thresholds

To characterize the FNR thresholds, we investigated the response of O<sub>3</sub> to emission perturbations using the GEOS-Chem model. GEOS-Chem is a three-dimensional chemical transport model driven by assimilated meteorological observations from the Goddard Earth Observing System (GEOS) of the NASA Global Modeling and Assimilation Office (GMAO) (<http://www.geos-chem.org>). To simulate O<sub>3</sub>, HCHO, and NO<sub>2</sub> for the year 2022, we used the high-performance GEOS-Chem (GCHP) model, version 14.4.0 (The International GEOS-Chem User Community, 2024). GCHP is described by Eastham et al. (2018). Improved advection, resolution, performance, and community access are described by Martin et al. (2022). In the current study, we configured four model runs.

For Run-1, global anthropogenic emissions were based on the Community Emissions Data System version 2 (CEDSV2) (McDuffie et al., 2020). We used the Regional Emission inventory in ASia version 3.2.1 (REASv3.2.1) (Kurokawa and Ohara, 2020), as the regional anthropogenic emissions override the global anthropogenic emissions for Japan. Biomass burning emissions were taken from the Global Fire Emissions Database version 4 (GFED4) (Van Der Werf et al., 2017). Additionally, dust, sea salt aerosol, soil NO<sub>x</sub>, lightning NO<sub>x</sub>, and biogenic VOCs emissions were computed offline (Weng et al., 2020). All emissions were configured at run-time using Harmonized Emissions Component (HEMCO, version 3.9.3) (Lin et al., 2021). Table S2 provides a detailed description of the emission inventories used in the model simulation. For meteorology, we used MERRA-2 (0.5° × 0.625°), a global atmospheric reanalysis data product. The full-chem model simulations use chemical mechanism kinetics following JPL/IUPAC recommendations (Bates et al., 2024). Photolysis frequencies for stratospheric and tropospheric chemistry are calculated with Cloud-J v7.7.3 (Prather, 2015). Stratospheric chemistry is represented by a linear chemistry mechanism, the Linoz algorithm (McLinden et al., 2000). The Linoz stratospheric chemistry package is recommended for GEOS-Chem simulations of O<sub>3</sub>. More details on the chemical mechanisms are available at <http://www.geos-chem.org>. In our study, the simulations were run using a 10-minute time step for chemistry and a 5-minute time step for transport. Moreover, we applied the grid-stretching capability to focus on the Japan region. The grid-stretching procedure followed Bindle et al. (2021), with an initial cubed-sphere grid of C90, a target latitude of 37°, a target longitude of 137°, and a stretch factor of 4. This procedure yielded an average horizontal resolution of 27.78 km over Japan. The simulation generated the vertical extent from the surface to approximately 80 km with a 72 vertical-layer grid. Surface concentrations were obtained from the first model layer. The tropospheric column and the stratospheric column were separated using tropopause information.

165 Furthermore, this troposphere-stratosphere distribution was used to derive the tropospheric column from the Pandora direct-sun observations.

Run-2 was the same as Run-1 but with all anthropogenic HCHO emissions turned off. Secondary HCHO reflects the VOCs activity through photolysis reactions. Previous studies have highlighted the importance of separating secondary HCHO from anthropogenic HCHO for a more accurate interpretation of the FNR (Hong et al., 2022; Xing et al., 2022; Xue et al., 2022).  
170 By comparing Run-1 and Run-2, we determined the contribution of primary HCHO and excluded it from the FNR calculation.

Run-3 and Run-4 were the same as Run-2 but with a 20 % reduction in regional NO<sub>x</sub> and VOC emissions, respectively. Ozone concentrations result from both in situ photochemical creation and external transport processes (Hong et al., 2022; Qian et al., 2024). A key advantage of the model-based method is that it allows us to exclude external transport processes, leading to a more precise classification of the O<sub>3</sub> chemical regime. The external O<sub>3</sub> transport influence was eliminated by subtracting  
175 Run-3 or Run-4 from Run-2. This step further reflects the response of O<sub>3</sub> to changes in NO<sub>x</sub> and VOCs. Figure S1 shows an example of the surface O<sub>3</sub> response to VOC and NO<sub>x</sub> emission reductions, resulting from GEOS-Chem simulations. Both negative and positive O<sub>3</sub> changes were observed in response to NO<sub>x</sub> emission reduction. In contrast, VOC emission reduction consistently led to decreases in O<sub>3</sub> levels. The Greater Tokyo Metropolitan Area was strongly influenced by these emission perturbations.

180 Regarding the responses, the O<sub>3</sub> sensitivity regime was categorized following the method of Jin et al. (2017) and Jung et al. (2022). Instead of the term VOC-limited regime, here we used the term “RO<sub>x</sub>-limited regime” for more accuracy present for the radical-limited regime. A negative change in O<sub>3</sub> owing to NO<sub>x</sub> emission reduction indicates a RO<sub>x</sub>-limited regime. A NO<sub>x</sub>-limited regime is defined when the positive change in O<sub>3</sub> owing to VOC emission reduction is smaller than that from NO<sub>x</sub> emission reduction. The FNR threshold values for RO<sub>x</sub>-limited and NO<sub>x</sub>-limited regimes were determined as those  
185 corresponding to the 95<sup>th</sup> percentile of the cumulative probability distribution for each regime.

### 3. Results and discussion

#### 3.1 Model simulations of HCHO, NO<sub>2</sub>, and O<sub>3</sub>

##### 3.1.1 Comparison with in situ and Pandora measurements

The correlation statistics between the GEOS-Chem simulations (Run-1) and in situ measurements are shown in Fig. 1, and  
190 those with Pandora are shown in Fig. 2. The GEOS-Chem simulations underestimated the surface HCHO concentrations, with a slope of 0.24, a correlation coefficient (R) of 0.32, and a root mean square error (RMSE) of 2,14 ppbv. Meanwhile, the GEOS-Chem overestimated the surface NO<sub>2</sub> concentrations, with a slope of 1.34, R = 0.48, and RMSE = 14.65 ppbv. However, the GEOS-Chem simulations aligned better with the Pandora tropospheric column densities. Specifically, the correlation coefficients between GEOS-Chem and Pandora for HCHO and NO<sub>2</sub> were 0.51 and 0.56, respectively, for Sapporo, 0.87 and  
195 0.72 for Tsukuba-NIES, 0.78 and 0.54 for Tokyo-TMU, and 0.69 and 0.70 for Fukuoka. The RMSE varied from 2.99 to 5.93 Pmolec cm<sup>-2</sup> for HCHO and from 2.11 to 5.71 Pmolec cm<sup>-2</sup> for NO<sub>2</sub>. The surface conditions are likely more complex compared to the tropospheric column, which could explain why the GEOS-Chem model imperfectly captured the surface characteristics. Additionally, the local emission inventory implemented in the model was based on the year 2015, which might cause a significant bias in the model results. The diurnal cycles of HCHO and NO<sub>2</sub> simulated by the GEOS-Chem model were  
200 compared with in situ measurements (Fig. S2) and Pandora (Fig. S3). The GEOS-Chem model successfully reproduced the surface diurnal cycle of HCHO. For surface NO<sub>2</sub>, the simulation captured the diurnal cycle in October quite well, but dramatically overestimated NO<sub>2</sub> concentrations in July. Both the Pandora observations and the GEOS-Chem simulations showed a midday decrease in tropospheric NO<sub>2</sub> columns. The GEOS-Chem model also simulated the growth in HCHO from

the morning; however, it showed a slight decrease after 2:00 PM. A larger difference between the model and Pandora was  
 205 observed at Tokyo-TMU, where primary HCHO emissions are significant.

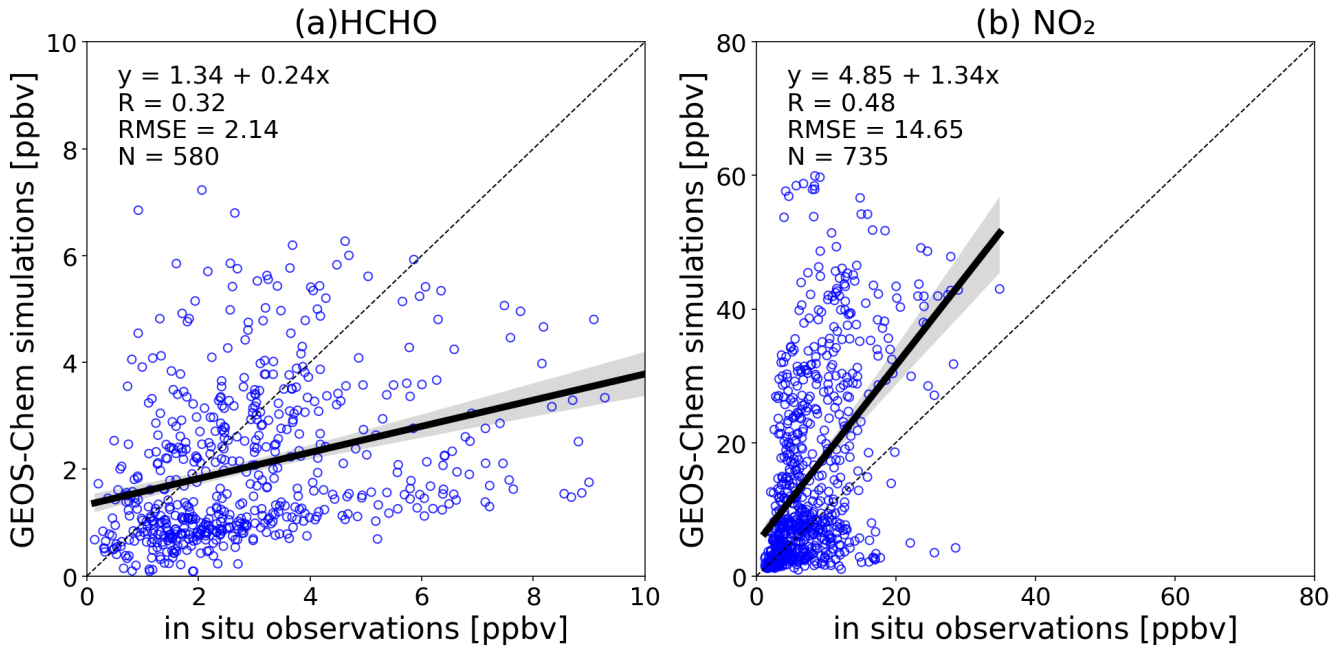
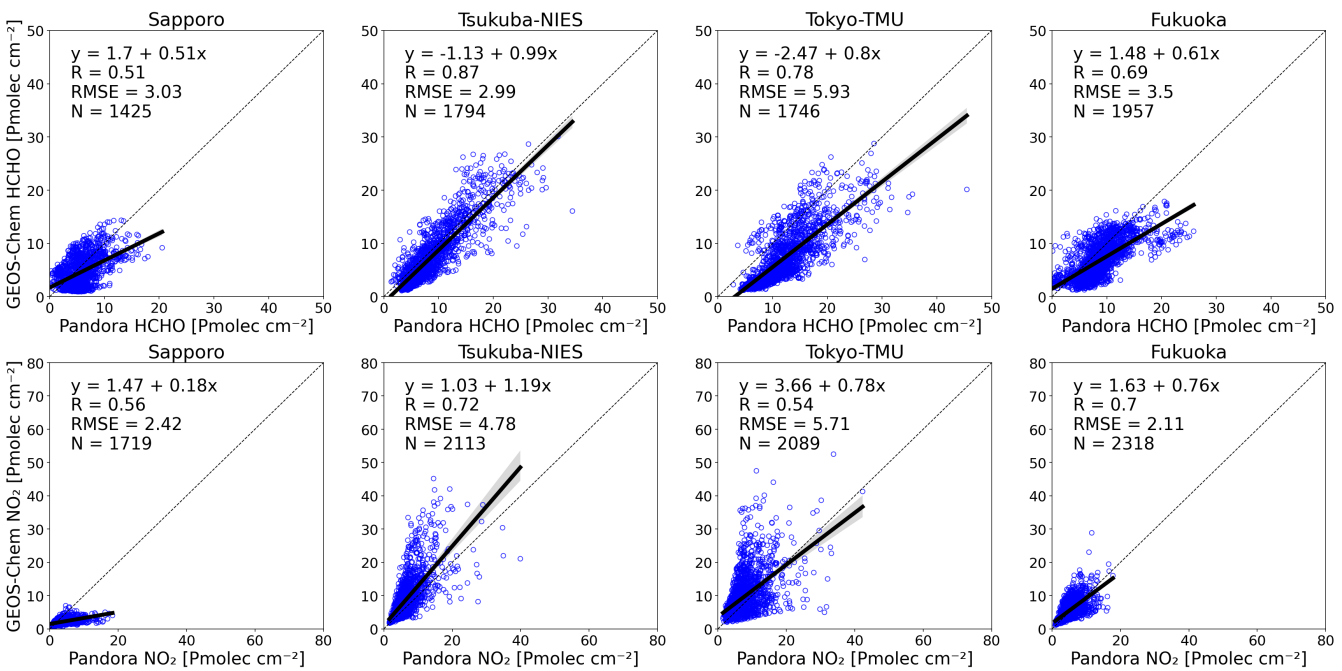


**Figure 1: Scatter plots of the surface HCHO (a) and NO<sub>2</sub> (b) comparing in situ measurements with GEOS-Chem model simulation at Tokyo-TMU. The y-axis represents GEOS-Chem simulations, and the x-axis represents in situ observations. The dashed line indicates the 1:1 line.**



210

**Figure 2: Scatter plots of tropospheric vertical column densities of HCHO (top panels) and NO<sub>2</sub> (bottom panels) between the Pandora direct-sun measurements and GEOS-Chem model simulations. The dashed line indicates the 1:1 line.**

For surface O<sub>3</sub>, we compared the GEOS-Chem model performance with in situ measurements from nearby air monitoring  
 stations at the four Pandora locations. The GEOS-Chem simulation was able to reproduce the inverted U-shaped pattern of O<sub>3</sub>  
 215 but showed positive biases (15–25 ppbv) (Fig. 3). The O<sub>3</sub> depletion during nighttime was not well generated by the GEOS-  
 Chem model, resulting in overestimated concentrations during photochemical periods. The faster nighttime depletion rate of  
 O<sub>3</sub> at Tokyo-TMU and Tsukuba-NIES suggests stronger deposition, which was not reflected by the model simulation. High  
 positive biases in surface O<sub>3</sub> have been reported in the literature (Travis et al., 2016; Travis and Jacob, 2019). The diurnal  
 variations in mixed-layer dynamics and ozone deposition velocities in the model are one of the key factors contributing to this  
 220 bias (Travis and Jacob, 2019). However, GEOS-Chem generally captured the observed variations in daytime O<sub>3</sub>, such as large

fluctuations at Tokyo-TMU and Tsukuba-NIES, and narrower variations at Fukuoka and Sapporo. The agreement between model simulation and in situ measurements was moderate, with an R of 0.56, 0.61, 0.53, and 0.59 for Sapporo, Tsukuba-NIES, Tokyo-TMU, and Fukuoka, respectively. Overall, the GEOS-Chem model could capture O<sub>3</sub> production at the study locations, indicating its suitability for investigating the O<sub>3</sub> sensitivity regime.

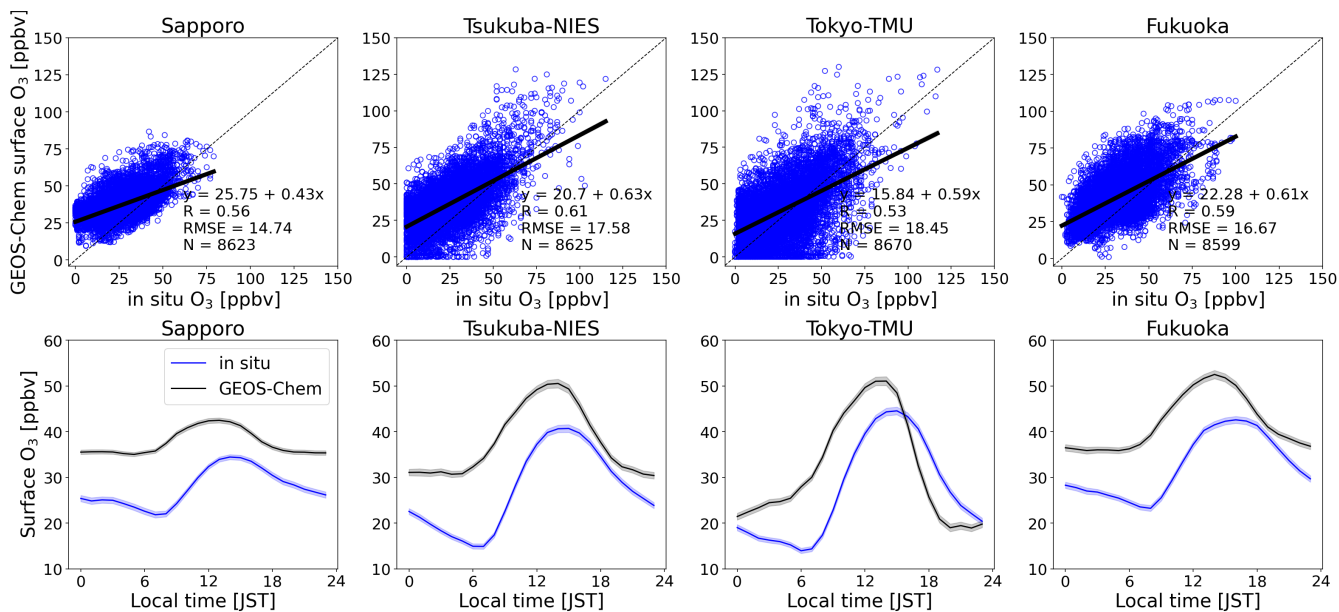


**Figure 3: Comparison of hourly surface O<sub>3</sub> between the GEOS-Chem model and in situ measurements at the study locations. The top-row panels show scatterplots with linear regression equations. The bottom-row panels present the diurnal cycles of surface O<sub>3</sub>, with shaded error bands indicating  $\pm 1$  standard error.**

### 3.1.2 Contribution of secondary HCHO

230 Table 1 shows the contributions of secondary HCHO at the study locations, derived from the GEOS-Chem simulations. We only considered daytime simulation from 8:00 to 16:00, when photochemical reactions actively occur. Basically, secondary HCHO contributed the majority at the surface level, with values of 86 %, 87 %, 76 %, and 90 % at Sapporo, Tsukuba-NIES, Tokyo-TMU, and Fukuoka, respectively. The contribution of primary HCHO was slightly higher at Tokyo-TMU (24 %). The secondary HCHO contribution increased in summer and decreased in winter. A diurnal variation of the contribution of secondary HCHO was observed, with the highest contribution around noon (not shown). For the tropospheric column, the seasonal contribution of secondary HCHO remained consistent. Additionally, the secondary HCHO contribution increased with altitude (Fig. S4a). The contribution at altitudes above 2 km was almost entirely attributed to secondary formation. This vertical distribution depends on primary emission sources, VOC oxidation, and photolysis rates. The higher photolysis frequency above 2 km compared to surface (Fig. S4b) therefore enhanced VOC oxidation as well as the magnitude of O<sub>3</sub> production. Secondary HCHO effectively represents a proxy for VOC reactivity (Su et al., 2019; Xue et al., 2022). For more accurate FNR calculation, these secondary HCHO contributions from the model simulations were adopted for both in situ and Pandora measurements. The FNR using secondary HCHO is referred to as FNR<sub>sec</sub>. This approach is particularly important in areas with a high contribution of primary sources of HCHO, for example, urban and industrial areas.

245 **Table 1: Contribution of secondary HCHO (%) at the surface level and in the tropospheric columns, obtained from the GEOS-Chem model simulation at the JPN sites. The statistical values were considered only for 8-hour daytime simulations (8:00 to 16:00).**

Location		Spring	Summer	Fall	Winter	Annual average
Sapporo	Surface	89 ± 13	98 ± 1	91 ± 9	65 ± 15	86 ± 17
	Tropospheric column	98 ± 2	99 ± 0	98 ± 2	93 ± 3	97 ± 3
Tsukuba-NIES	Surface	89 ± 11	96 ± 4	91 ± 10	74 ± 16	87 ± 14
	Tropospheric column	96 ± 4	99 ± 1	97 ± 3	90 ± 6	95 ± 5

<b>Tokyo-TMU</b>	Surface	76 ± 16	92 ± 8	77 ± 19	58 ± 22	76 ± 21
	Tropospheric column	91 ± 5	97 ± 2	93 ± 5	85 ± 8	92 ± 7
<b>Fukuoka</b>	Surface	90 ± 9	97 ± 3	92 ± 8	79 ± 13	90 ± 11
	Tropospheric column	97 ± 3	99 ± 0	98 ± 2	94 ± 3	97 ± 3

### 3.2 Overall levels of HCHO and NO<sub>2</sub>

#### 3.2.1 Surface levels

The diurnal plots of HCHO and NO<sub>2</sub> obtained from in situ measurements at the Tokyo-TMU site are shown in Fig. S2. Near the surface, HCHO concentrations fluctuated within a narrow range of a few ppbv throughout the day. The minimum occurred at mid night, while the peak was observed around noon (in July) or late afternoon (in October). HCHO concentrations are generally expected to be higher in summer due to enhanced photochemical reactions driven by stronger solar irradiance and increased biogenic VOCs emissions from the local flora (Irie et al., 2021). However, interestingly, we found negligible differences in surface HCHO concentrations between July and October. The mean HCHO concentrations in July and October were  $2.77 \pm 1.73$  and  $3.06 \pm 2.10$  ppbv, respectively.

Surface NO<sub>2</sub> concentrations were twice as high in October compared to July. In July, the NO<sub>2</sub> mixing ratio ranged from 0.90 to 21.10 ppbv, with an average of 5.98 ppbv. In October, the surface NO<sub>2</sub> ranged from 1.24 to 39.13 ppbv, with an average of 9.91 ppbv. Peaks in July were not clearly defined. In contrast, October showed a small peak in the morning and a larger one around 18:00, exhibiting traffic emissions, while minimum concentrations occurred at noon due to photochemical loss. The finding that the diurnal trend of NO<sub>2</sub> was opposite to that of HCHO can be explained by photochemical reactions. These diurnal cycles have been well documented in previous studies (Irie et al., 2011; Itahashi and Irie, 2022).

#### 3.2.2 Vertical column amounts

Figure 4 shows the variation in vertical column density (VCD) of HCHO measured by the Pandora spectrometer in 2022 at the study sites. The highest total VCD was observed at Tokyo-TMU, with a mean value of  $12.30 \pm 4.99$  Pmolec cm<sup>-2</sup>. The levels at Sapporo, Tsukuba-NIES, and Fukuoka were  $6.01 \pm 2.84$ ,  $8.97 \pm 5.05$ , and  $9.05 \pm 4.02$  Pmolec cm<sup>-2</sup>, respectively. According to the GEOS-Chem simulations, the contribution of primary HCHO at Tokyo-TMU was higher than that at the other study sites (Table 1), indicating that the elevated column amount at Tokyo-TMU was largely influenced by local emission of anthropogenic sources. Clearly, the HCHO column amounts tended to be higher in summer and lower in winter. As discussed in Sect. 3.2.1, the difference in surface HCHO concentrations between July and October at Tokyo-TMU was not statistically significant. However, the total HCHO VCD measured by Pandora in July ( $16.47 \pm 5.05$  Pmolec cm<sup>-2</sup>) was 1.5 times higher than that in October ( $10.90 \pm 2.05$  Pmolec cm<sup>-2</sup>). Additionally, we found a strong relationship between column densities and surface concentrations, with a correlation of 0.7 for HCHO (Fig. S5). The correlation slope was about three times higher in July than in October, likely due to enhanced HCHO production at higher altitudes during summer. This suggests that column information is essential and complement to surface measurements for fully representing atmospheric HCHO.

The lower tropospheric column (up to an altitude of 3 km) of HCHO (obtained from the sky-scan mode) accounted for 59.14 ± 18.83 % at Sapporo, 65.86 ± 14.84 % at Tsukuba-NIES, 49.04 ± 16.76 % at Tokyo-TMU, and 62.27 ± 16.66 % at Fukuoka, relative to the total column amount (obtained from the direct-sun mode). This lower tropospheric contribution was dominant in summer, ranging from 61.27 % to 71.65 %, and decreased in winter, varying from 32.92 % to 54.93 %. However, it should be noted the error budget in Pandora direct-sun HCHO (Spinei et al., 2018). This error budget can overestimate the total column density. The diurnal cycle of the tropospheric HCHO column is shown in Fig. S3. The tropospheric column measured by Pandora exhibited a continuous increase from the morning to the afternoon. The accumulation of HCHO and the decreasing rate of photolysis in the afternoon can explain this daily cycle of HCHO (Souri et al., 2023b; Zhang et al., 2021).

In contrast to the HCHO trend, the NO<sub>2</sub> column amounts reached their minimum in summer (Fig. 4). Tokyo-TMU was also polluted with NO<sub>2</sub>, with an average of  $9.73 \pm 4.99$  Pmolec cm<sup>-2</sup> ( $12.55 \pm 6.52$  Pmolec cm<sup>-2</sup> in winter and  $6.80 \pm 2.17$  Pmolec cm<sup>-2</sup> in summer), followed by Tsukuba-NIES with an average of  $8.33 \pm 3.88$  Pmolec cm<sup>-2</sup> ( $8.83 \pm 4.42$  Pmolec cm<sup>-2</sup> in winter and  $7.84 \pm 2.50$  Pmolec cm<sup>-2</sup> in summer). The total NO<sub>2</sub> VCDs at Sapporo and Fukuoka were  $7.92 \pm 4.45$  Pmolec cm<sup>-2</sup> and  $7.22 \pm 3.01$  Pmolec cm<sup>-2</sup>, respectively. The lower tropospheric column contributed  $51.38 \pm 20.86$  %,  $53.95 \pm 18.06$  %,  $59.55 \pm 16.79$  %, and  $56.29 \pm 18.83$  % to the total column at Sapporo, Tsukuba-NIES, Tokyo-TMU, and Fukuoka, respectively. We also found good agreement for NO<sub>2</sub> between lower tropospheric column densities and surface concentrations, with a correlation of 0.6 (Fig. S5). The slope was similar in July and October, reflecting that NO<sub>2</sub> is mainly concentrated near the surface.

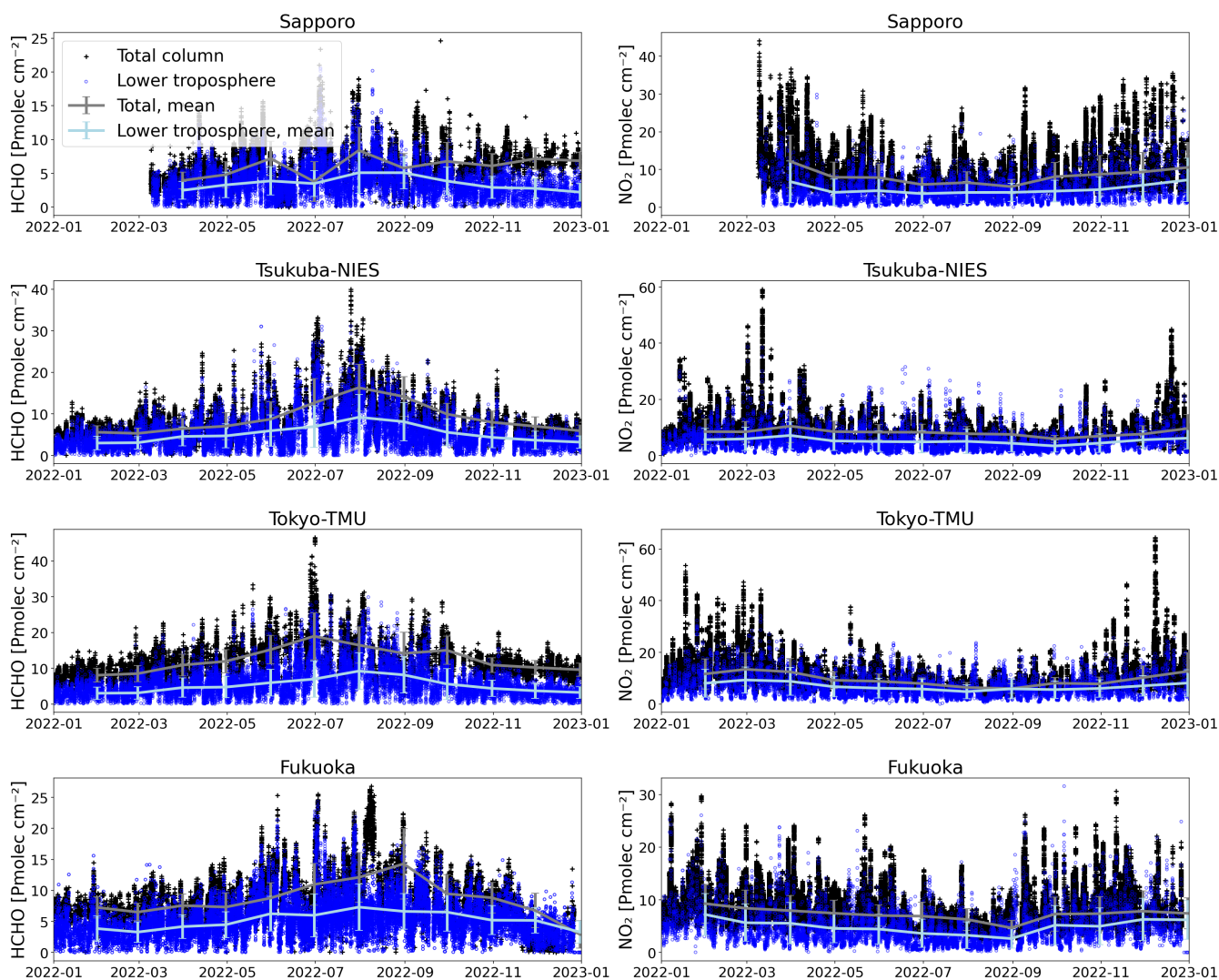
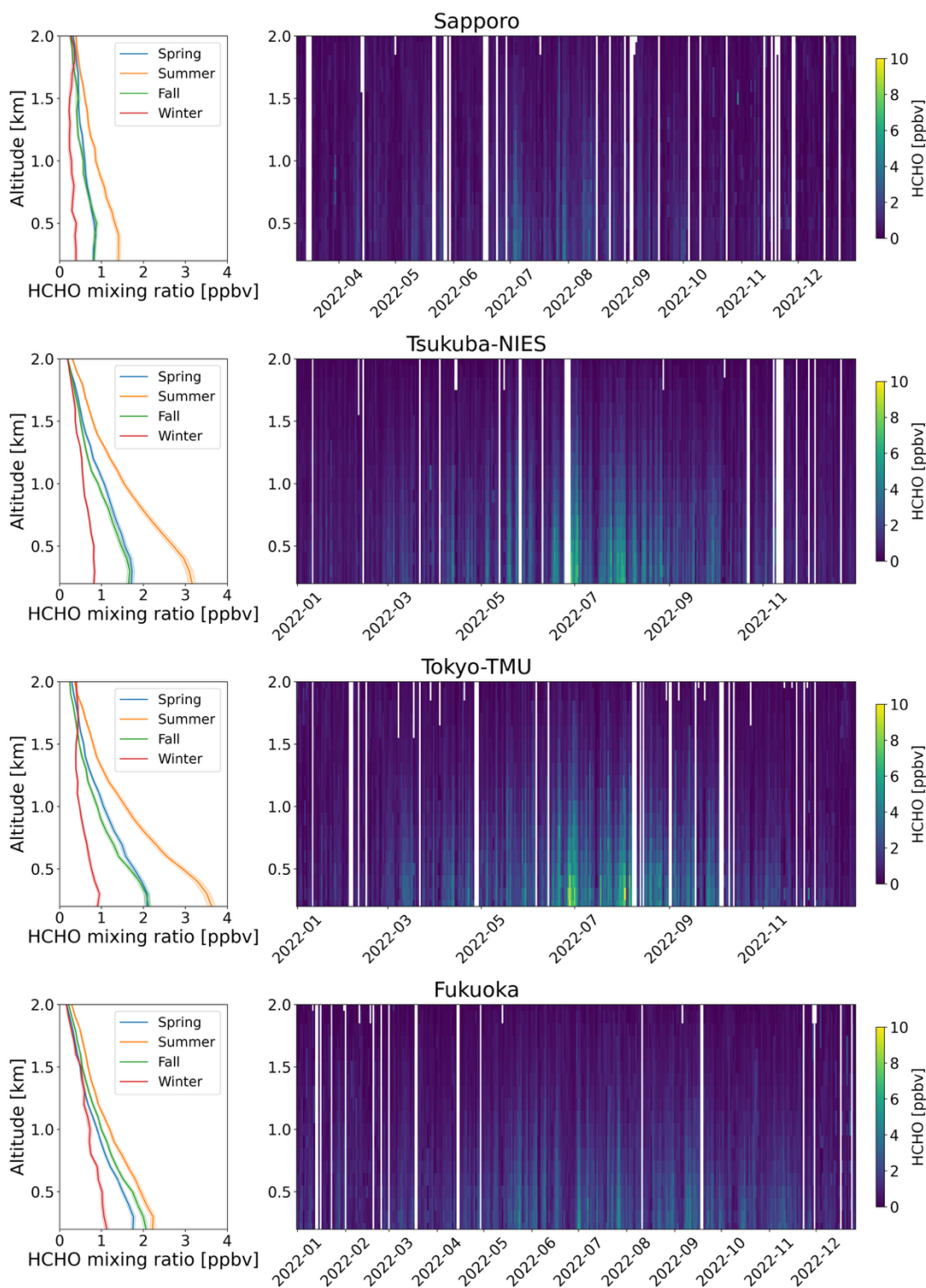


**Figure 4:** Time series plots of vertical column densities of HCHO (left column) and NO<sub>2</sub> (right column) at the study locations in 2022. Black plus signs represent total column densities derived from the Pandora direct-sun mode, whereas blue dots indicate lower tropospheric columns (up to an altitude of 3 km) derived from the Pandora sky-scan mode. Solid lines show monthly means, and error bars represent standard deviation. ( $1 \text{ Pmolec cm}^{-2} = 1 \times 10^{15} \text{ molecules cm}^{-2}$ ).

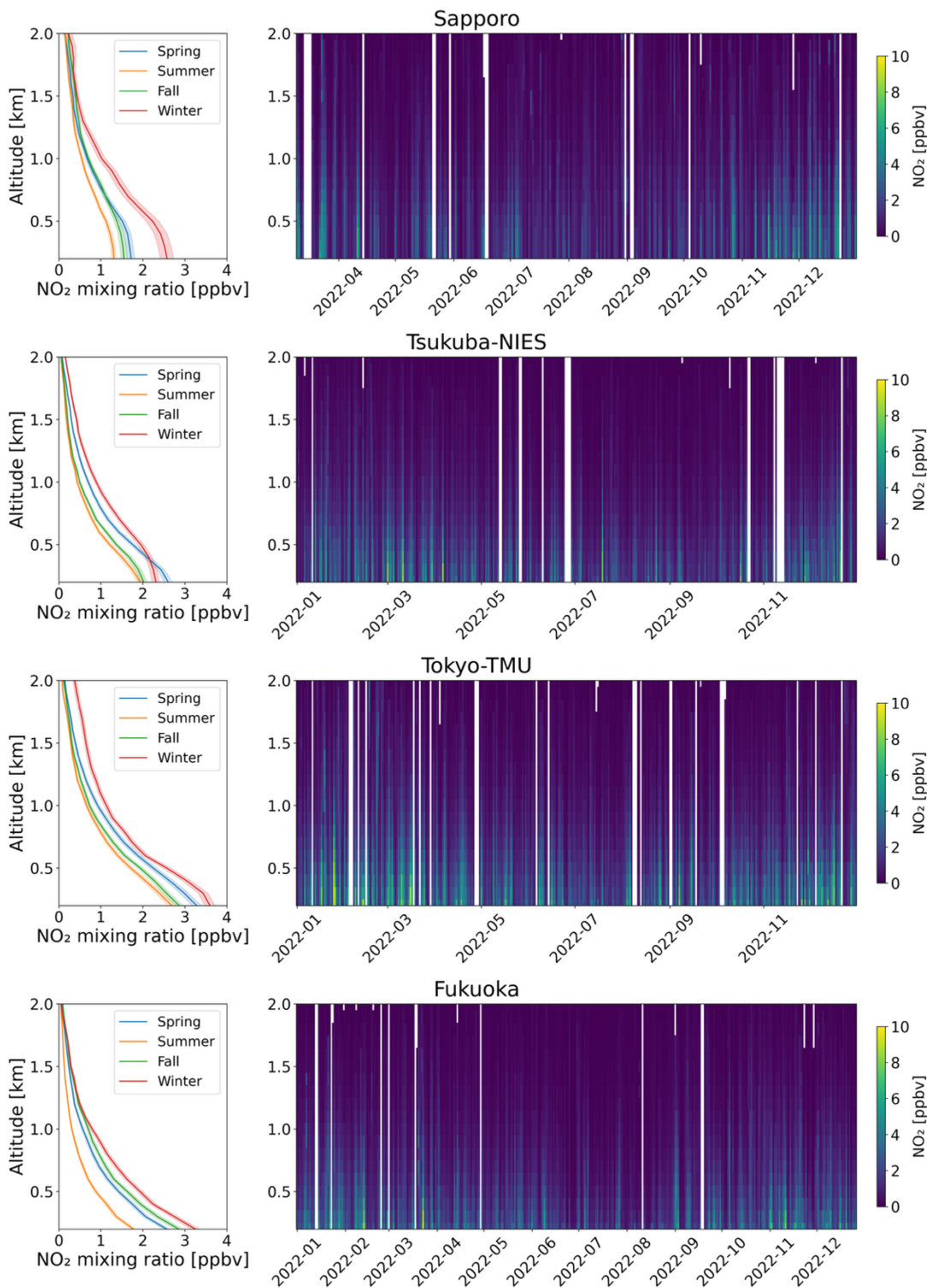
### 3.2.3 Vertical profiles

The Pandora sky-scan mode measures scattered sunlight at several angles, yielding the vertical profiles. The resolution of the vertical profiles depends on the number of scanning angles, referred to as elevation scan routines (i.e., detailed elevation scan and quick elevation scan). Here, we used detailed elevation scans around noon to investigate the vertical distribution of HCHO and NO<sub>2</sub>. The detailed elevation scan routine observes 14 angles without using filter and 12 angles using the U340 filter,

respectively (Rawat et al., 2025). We converted these partial vertical columns to mixing ratios, assuming well-mixed conditions in each layer and the ideal gas law. To obtain the seasonal vertical distributions of HCHO and NO<sub>2</sub>, after extrapolating into 0.1 km bins, the profiles were averaged by altitude. Since the altitudes of these four Pandora stations ranged from 45 to 135 m, and the maximum vertical sensitivity of the sky-scan mode was generally within 2 km, we only considered the vertical profile from 0.2 to 2 km. Figures 5 and 6 present the seasonal and time-series vertical profiles of HCHO and NO<sub>2</sub>, respectively.



310 **Figure 5: Seasonal (first column) and time series (second column) vertical profiles of HCHO derived from the Pandora sky-scan observations around noon ( $12:00 \pm 2:00$ ). The seasonal vertical profiles are shaded with error bands indicating  $\pm 1$  standard error. Color bars exhibit HCHO mixing ratio.**



315 **Figure 6: Seasonal (first column) and time series (second column) vertical profiles of NO<sub>2</sub> derived from the Pandora sky-scan observations around noon (12:00 ± 2:00). The seasonal vertical profiles are shaded with error bands indicating ±1 standard error. Color bars exhibit NO<sub>2</sub> mixing ratio.**

The HCHO productions were significantly enhanced during summer due to stronger solar intensity and increased biogenic VOCs emissions such as isoprene. Secondary HCHO is associated with isoprene emitted from vegetation (Ryan et al., 2023). Isoprene emissions exhibit a markedly positive exponential relationship with temperature (Ryan et al., 2023; Wang et al., 2024). At higher temperatures in summer, more isoprene is emitted, which triggers the formation of secondary HCHO. The higher HCHO production at Tsukuba-NIES and Tokyo-TMU compared to Fukuoka suggests that, in addition to biogenic VOCs, anthropogenic VOCs play an important role in HCHO production (Fig. S6). Anthropogenic VOC emission accounted for 20 % of the total emission at the two locations. The summertime increase in anthropogenic VOCs emissions is likely driven by enhanced evaporation processes (Wu et al., 2024). The vertical variation of HCHO appeared to be relatively heterogeneous

320

in winter. However, we found less significant changes in the seasonal profiles at the highest latitude site (Sapporo). Vertically, HCHO formation was observed up to 2 km, which is consistent with previous studies (Lin et al., 2022; Shi et al., 2025b). HCHO extended to higher altitudes could be attributed to vertical and horizontal transport and chemistry (Souri et al., 2023c). For a more accurate FNR analysis, it is essential to consider not only surface but also elevated measurements (Souri et al., 2025).

The NO<sub>2</sub> distributions more rapidly decreased with increasing altitude compared to HCHO. Unlike HCHO, the bulk of NO<sub>2</sub> was generally concentrated below 1 km because NO<sub>x</sub> emissions are mainly near the surface (i.e., traffic). Normally, the vertical NO<sub>2</sub> profile was enhanced in winter. However, we also observed several spikes of NO<sub>2</sub> during summer at Tsukuba-NIES. Generally, NO<sub>2</sub> concentrations are low in summer because of photochemical loss. The enhanced NO<sub>2</sub> profiles observed at Tsukuba-NIES during summer could be attributed to the transport of emissions from surrounding regions. Irie et al. (2021) reported that summertime air masses passing over Tokyo Bay area and reaching Tsukuba lead to a greater O<sub>3</sub> concentrations at this site.

To investigate whether any external transport affected the vertical profiles, we applied the Hybrid Single-Particle Lagrangian Integrated Trajectory (HYSPLIT) model for the Tsukuba-NIES case. The model, developed by the National Oceanic and Atmospheric Administration (NOAA) Air Resources Laboratory (ARL), has been widely used for atmospheric trajectory and dispersion calculations (Stein et al., 2015). We simulated 48-hour backward trajectories for the year 2022, with endpoints at 13:00 local time (JST) at Tsukuba-NIES, as a case study. The backward trajectories were assigned into four clusters: c1, c2, c3, and c4. The number of clusters was optimized using total spatial variance (TSV) analysis. The cluster frequencies were 15 %, 40 %, 36 %, and 9 % for c1, c2, c3, and c4, respectively (Fig. S7). Figure S8 shows the vertical profiles of NO<sub>2</sub> at Tsukuba-NIES during summer as a function of air mass clusters. During summer, cluster c1 occurred on only one day, clusters c2, c3, and c4 occurred on 34, 33, and 24 days, respectively. Thus, we observed elevated in NO<sub>2</sub> profiles during cluster c4, in which air masses passed through urban Tokyo and industrial areas, transporting anthropogenic pollutants to the Tsukuba-NIES site. This suggests that external pollution transport affected the vertical distributions of NO<sub>2</sub>, and consequently, O<sub>3</sub> production.

### 3.3 Identification of the O<sub>3</sub> sensitivity regime

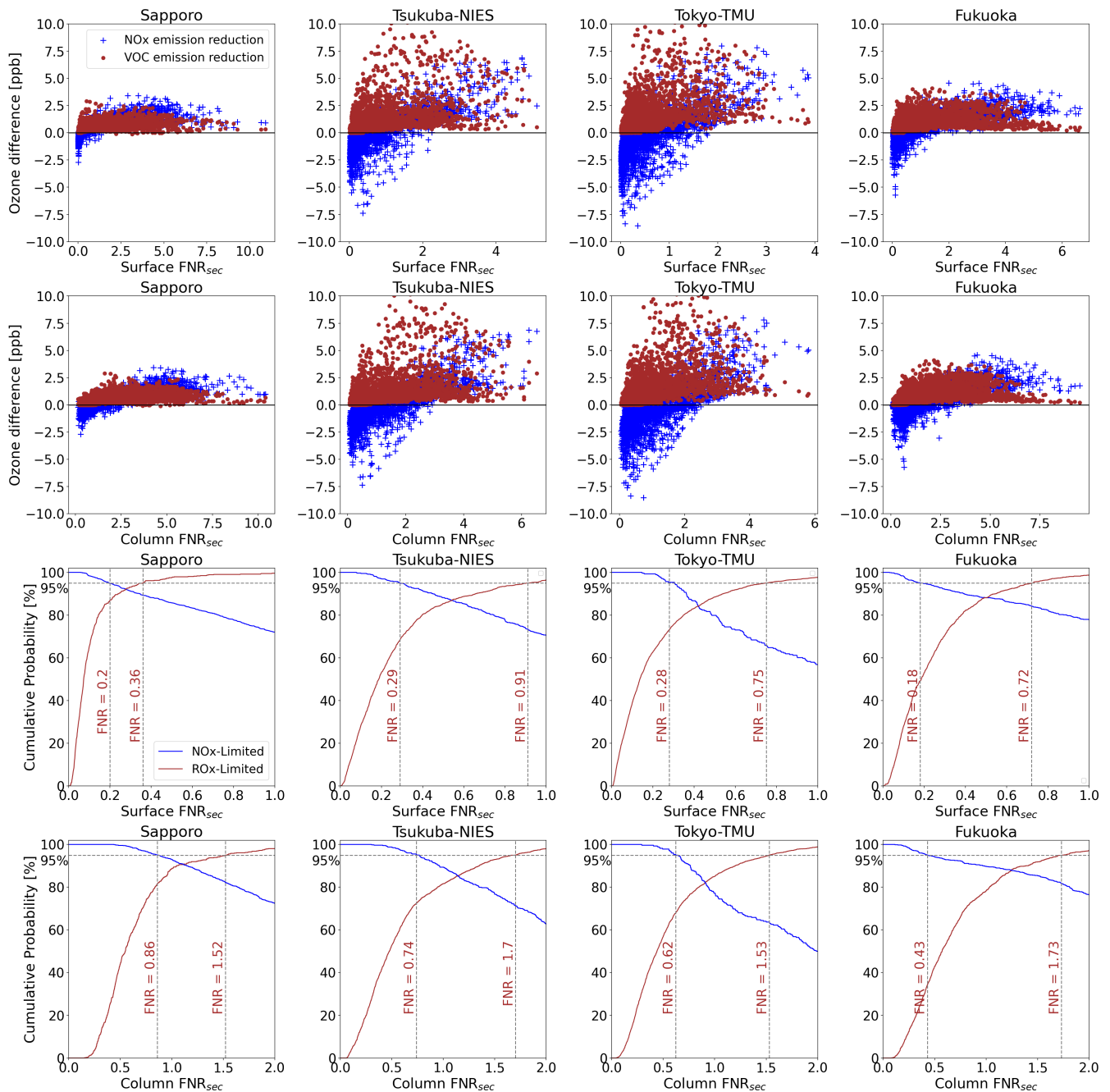
The O<sub>3</sub>, HCHO, and NO<sub>2</sub> outputs from the GEOS-Chem model simulations were utilized to identify the O<sub>3</sub> sensitivity regime (Fig. 7). From the scatter plots, the responses of surface O<sub>3</sub> to NO<sub>x</sub> and VOC emission reductions at Sapporo and Fukuoka were within 5 ppbv, which were less pronounced than those at Tsukuba-NIES and Tokyo-TMU (within 10 ppbv). A positive O<sub>3</sub> difference indicates that the emission reduction results in a decrease in surface O<sub>3</sub>. Conversely, a negative difference means that the emission reduction enhances surface O<sub>3</sub> concentrations. In our study, generally, VOC emission reductions led to a decrease in surface O<sub>3</sub> concentrations. NO<sub>x</sub> emission reductions could either decrease O<sub>3</sub> through photochemical reaction or increase it due to reduced LNO<sub>x</sub> processes.

The FNR<sub>sec</sub> threshold values were determined using both surface and column information (Fig. 7, cumulative graphs). Based on surface FNR<sub>sec</sub>, the RO<sub>x</sub>-limited conditions were distinguished with thresholds of FNR<sub>sec</sub> <0.2 for Sapporo, <0.29 for Tsukuba-NIES, <0.28 for Tokyo-TMU, and <0.18 for Fukuoka. The NO<sub>x</sub>-limited regimes were associated with FNR<sub>sec</sub> > 0.36 for Sapporo, and >0.91, >0.75, and >0.72 for Tsukuba-NIES, Tokyo-TMU, and Fukuoka, respectively. The surface FNR<sub>sec</sub> thresholds were generally lower than the column FNR<sub>sec</sub>. The finding of higher column FNR is consistent with previous studies (Jin et al., 2017; Souri et al., 2023a). The column FNR<sub>sec</sub> thresholds for the RO<sub>x</sub>-limited regimes and NO<sub>x</sub>-limited regimes at the Sapporo site were <0.86 and >1.52, respectively. The corresponding column FNR<sub>sec</sub> threshold ranges for Tsukuba-NIES, Tokyo-TMU, and Fukuoka were 0.74–1.7, 0.62–1.53, and 0.43–1.73, respectively. The transitional regime seemed to occur over a wider range of column FNR<sub>sec</sub> values at lower latitudes (e.g., Fukuoka) compared to higher latitudes (e.g., Sapporo). The differences between surface and tropospheric column FNR<sub>sec</sub> could be attributed to the vertical

characteristics of HCHO and NO<sub>2</sub>. NO<sub>2</sub> molecules were concentrated near the surface, while HCHO was present in the higher layers. As a result, surface FNR<sub>sec</sub> did not account for HCHO at higher layers, leading to lower threshold values. The surface and column FNR<sub>sec</sub> thresholds identified in this study are consistent with those reported by Jin et al. (2017) for East Asia (Table 2).

370 For the column, the transition range for Sapporo was defined as 0.86–1.52 where the cumulative probability of NO<sub>x</sub>-limited and RO<sub>x</sub>-limited condition reached 95 %, corresponding to a 5 % probability of misclassification. Consequently, 15 % of NO<sub>x</sub>-limited and 15 % of RO<sub>x</sub>-limited conditions were incorrectly classified as transitional (Fig. 7). Similarly, the probabilities of misclassifying NO<sub>x</sub>-limited and RO<sub>x</sub>-limited conditions as transitional were 20 % and 25 %, respectively, for Tsukuba-NIES, 35 % and 25 % for Tokyo-TMU, and 15 % and 60 % for Fukuoka. Notably, the probability of misclassification of RO<sub>x</sub>-limited condition at Fukuoka was higher than at the other locations. Because we simulated for the year 2022, this uncertainty could be reduced by extending the model simulations to longer time periods.

375



380 **Figure 7: Response of surface O<sub>3</sub> to NO<sub>x</sub> and VOC emission perturbations resulting from the GEOS-Chem simulations. The scatter plots depict the O<sub>3</sub> difference between GEOS-Chem Run-2 and Run-3 (blue), and between Run-2 and Run-4 (brown), as a function of surface FNR<sub>sec</sub> (first row) and tropospheric column FNR<sub>sec</sub> (second row). The VOC-limited regime was associated with negative**

change in O<sub>3</sub> due to NO<sub>x</sub> emission reduction. The NO<sub>x</sub>-limited regime was identified when the positive change in O<sub>3</sub> due to VOC emission reductions was smaller than that from NO<sub>x</sub> emission reductions. Line plots show the cumulative probability of NO<sub>x</sub>-limited (blue) and VOC-limited (brown) conditions as a function of surface FNR<sub>sec</sub> (third row) and tropospheric column FNR<sub>sec</sub> (fourth row). The FNR<sub>sec</sub> threshold values (vertical dashed lines) for VOC-limited and NO<sub>x</sub>-limited regimes were determined as those corresponding to the 95<sup>th</sup> percentile (horizontal dashed lines) of the cumulative probability distribution for each regime.

Table 2 presents the column FNR regime thresholds related to surface O<sub>3</sub> sensitivity from previous studies. These threshold values vary depending on the methodology, geographic region, and atmospheric conditions. The FNR thresholds using both primary and secondary HCHO (FNR<sub>total</sub>) are higher than those using only secondary HCHO (FNR<sub>sec</sub>). The transitional regimes are reported for a column FNR<sub>total</sub> of 2.5–4.0 in Guangzhou, China (Hong et al., 2022), and 1.6–2.6 in United States (Jung et al., 2022), whereas the column FNR<sub>sec</sub> thresholds identified in our study were lower than 2. Column FNR regime threshold values are useful for examining global O<sub>3</sub> production, as both satellite and ground-based remote sensing techniques offer extensive spatial coverage (Inoue et al., 2019; Ryan et al., 2023; Santiago et al., 2021).

**Table 2: Comparison of column FNR threshold values for O<sub>3</sub> sensitivity in previous studies using different methods.**

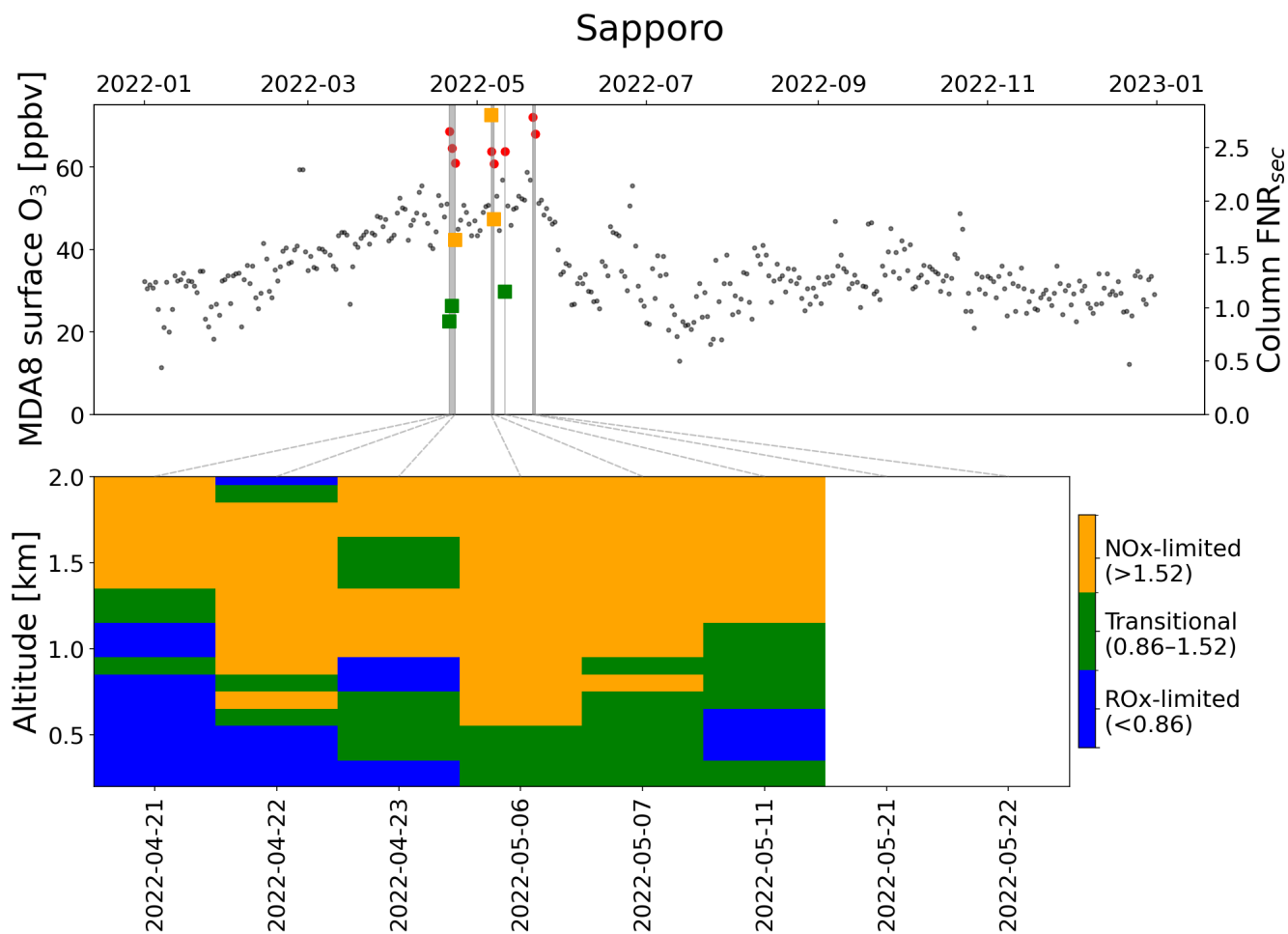
Study area	Indicator	Method	FNR <sub>total</sub> threshold	FNR <sub>sec</sub> threshold	Reference
			values	values	
North America	Column FNR <sub>total</sub>	GEOS-Chem model	0.9–1.4	-	(Jin et al., 2017)
Europe	Column FNR <sub>total</sub>	GEOS-Chem model	0.9–1.2	-	(Jin et al., 2017)
East Asia	Column FNR <sub>total</sub>	GEOS-Chem mode	0.9–1.6	-	(Jin et al., 2017)
United States	Column FNR <sub>total</sub>	CMAQ model	1.6–2.6	-	(Jung et al., 2022)
Guangzhou, China	Column FNR <sub>total</sub>	Polynomial fit of O <sub>3</sub>	2.5–4.0	-	(Hong et al., 2022)
Sapporo	Column FNR <sub>sec</sub>	GEOS-Chem model	-	0.86–1.52	This study
Tsukuba-NIES	Column FNR <sub>sec</sub>	GEOS-Chem model	-	0.74–1.70	This study
Tokyo-TMU	Column FNR <sub>sec</sub>	GEOS-Chem model	-	0.62–1.53	This study
Fukuoka	Column FNR <sub>sec</sub>	GEOS-Chem model	-	0.43–1.73	This study

### 3.4 O<sub>3</sub> sensitivity during exceedance events

The diurnal and seasonal cycles of surface and column FNR are shown in Figs. S9 and S10. Surface FNR<sub>sec</sub> developed in the early morning and decreased in the afternoon. During the 8-hour daytime period (8:00 to 16:00), the average surface FNR<sub>sec</sub> was  $0.99 \pm 0.46$  in July and  $0.72 \pm 0.64$  in October. Using tropospheric vertical column densities derived from Pandora sky-scan observations, the column FNR<sub>sec</sub> exhibited a higher value compared to those from surface measurements. Like surface FNR<sub>sec</sub>, the tropospheric column FNR<sub>sec</sub> increased during the morning. The highest column FNR<sub>sec</sub> values were found during the summer months (JJA). In contrast, these values were normally below 1 in winter (DJF).

In this section, we analyze the O<sub>3</sub> formation sensitivity focusing on polluted days when the maximum daily 8-hour averaged surface O<sub>3</sub> (MDA8) exceeded 60 ppbv. We identified 8, 30, 38, and 43 exceedance events in 2022 at Sapporo, Tsukuba-NIES, Tokyo-TMU, and Fukuoka, respectively. During O<sub>3</sub> exceedance events, photochemical reactions were typically strong, allowing us to determine the sensitive regime with minimum biases. Because the model simulations did not reproduce surface NO<sub>2</sub> and HCHO as well as the column densities, we will focus only on column FNR. Although Pandora direct-sun mode provides highly accurate NO<sub>2</sub> measurements, the HCHO retrieval attains non-negligible error budget, which can cause more uncertainty and bias in the FNR. In contrast, Pandora sky-scan mode provides lower tropospheric columns of NO<sub>2</sub> and HCHO and yields lower uncertainty in the HCHO data product. Additionally, the sensitivity diagnosis within the boundary layer is better represent tropospheric O<sub>3</sub> production processes. Therefore, we discuss instead the column FNR<sub>sec</sub> derived from Pandora sky-scan observations which is sensitive to the boundary layer. We averaged available sky-scan observations around noon ( $12:00 \pm 2:00$ ), when photolysis rates are highest. Figures 8-11 present column FNR<sub>sec</sub> during O<sub>3</sub> polluted events at Sapporo, Tsukuba-NIES, Tokyo-TMU, and Fukuoka, respectively. The advantage of Pandora observations is the ability to examine

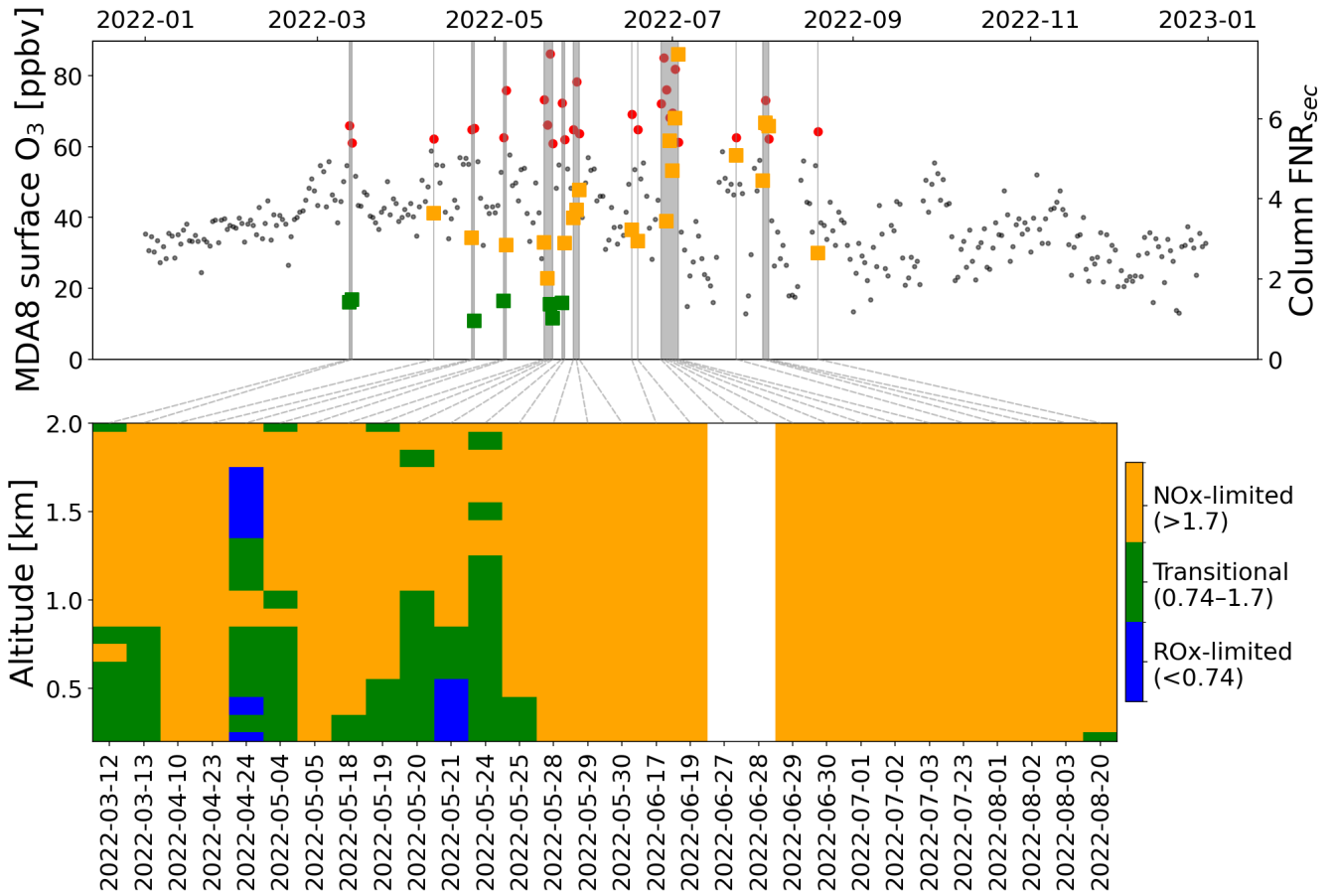
daily O<sub>3</sub> production in greater detail and investigate specific periods such as exceedance events. Based on the analysis of these  
415 events, policy strategies could be proposed to help mitigate O<sub>3</sub> pollution.



420 **Figure 8: Sensitivity analysis of O<sub>3</sub> during MDA8 exceedance events at Sapporo. The top panel presents MDA8 surface O<sub>3</sub>, with non-exceedance days indicated by black dots and exceedance days shown as red points with grey shadows. Squares depict the column FNR<sub>sec</sub> derived from Pandora sky-scan measurements around local noon (12:00 ± 2:00). The bottom panel illustrates the vertical formation sensitivity of O<sub>3</sub> corresponding to exceedance events. The squares and color bars are colored according to FNR<sub>sec</sub> threshold values determined from the GEOS-Chem model.**

At Sapporo, the O<sub>3</sub> concentrations increased during spring (Fig. 8). All eight events with MDA8 O<sub>3</sub> exceeding 60 ppbv occurred in April and May 2022. Pandora observations were unavailable on 21 and 22 May 2022. Given the transition range  
425 determined at Sapporo ( $0.86 < \text{FNR}_{\text{sec}} < 1.52$ ), the column FNR<sub>sec</sub> exhibited O<sub>3</sub> sensitivity in transitional and NO<sub>x</sub>-limited regime. Therefore, reducing NO<sub>x</sub> emission would be the optimal strategy for mitigating O<sub>3</sub> levels. The vertical sensitivity indicated that the RO<sub>x</sub>-limited regime was typically confined to the near surface layer during events classified as transitional using column FNR<sub>sec</sub>. Concurrently, the NO<sub>x</sub>-limited regime frequently formed aloft, whereas the transitional regime formed in the mid-levels. Figure S11 in the SI illustrates the corresponding HCHO and NO<sub>2</sub> profiles for these exceedance events.  
430 Higher concentration of NO<sub>2</sub> on 21 and 22 April, concentrated below 0.5 km, led to a RO<sub>x</sub>-limited regime within this layer. For events categorized as NO<sub>x</sub>-limited (6-7 May) according to the column FNR<sub>sec</sub>, the NO<sub>x</sub>-limited regime dominated at higher altitudes and expanded downward to the surface, while the RO<sub>x</sub>-limited regime retreated. Even during periods of high MDA8, the vertical profiles of both NO<sub>2</sub> and HCHO on 23 April and 6 May were low, suggesting that O<sub>3</sub> could be influenced by regional or vertical transport. This influence could be recognized using Pandora HCHO and NO<sub>2</sub> observations; however,  
435 further studies are needed to distinguish these events from local photochemical O<sub>3</sub> production.

## Tsukuba-NIES



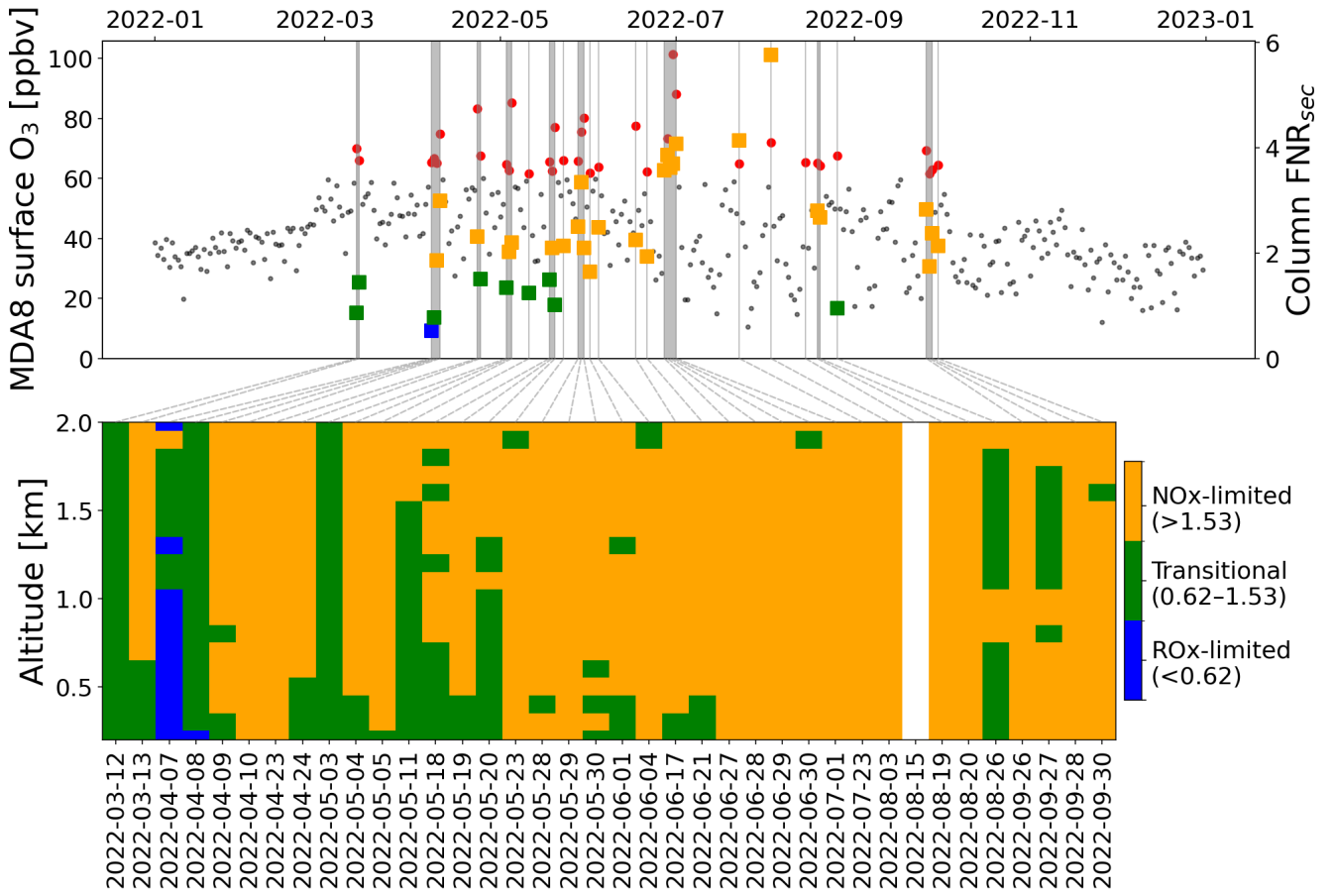
440

**Figure 9: Sensitivity analysis of O<sub>3</sub> during MDA8 exceedance events at Tsukuba-NIES.** The top panel presents MDA8 surface O<sub>3</sub>, with non-exceedance days indicated by black dots and exceedance days shown as red points with grey shadows. Squares depict the column FNR<sub>sec</sub> derived from Pandora sky-scan measurements around local noon (12:00 ± 2:00). The bottom panel illustrates the vertical formation sensitivity of O<sub>3</sub> corresponding to exceedance events. The squares and color bars are colored according to FNR<sub>sec</sub> threshold values determined from the GEOS-Chem model.

445

Figure 9 is similar to Figure 8, but for Tsukuba-NIES. Compare with Sapporo, more O<sub>3</sub> exceedance events were found at Tsukuba-NIES, with 30 events in 2022. These events primarily took place during spring and summer. Like the results at Sapporo, the column FNR<sub>sec</sub> exhibited transitional and NO<sub>x</sub>-limited conditions during spring events, whereas O<sub>3</sub> chemistry was almost entirely NO<sub>x</sub>-limited during summer events, likely due to substantial enhancement in HCHO production (Fig. S11). Regarding vertical sensitivity, we determined a lower probability of RO<sub>x</sub>-limited regime during the spring events. During summer events, O<sub>3</sub> formation sensitivity throughout the lower troposphere was consistently NO<sub>x</sub>-limited, consistent with the column FNR<sub>sec</sub> classification. Thus, emission policies focusing on continued reductions in NO<sub>x</sub> would effectively improve tropospheric O<sub>3</sub> pollution during summer.

# Tokyo-TMU



450

**Figure 10: Sensitivity analysis of O<sub>3</sub> during MDA8 exceedance events at Tokyo-TMU. The top panel presents MDA8 surface O<sub>3</sub>, with non-exceedance days indicated by black dots and exceedance days shown as red points with grey shadows. Squares depict the column FNR<sub>sec</sub> derived from Pandora sky-scan measurements around local noon (12:00 ± 2:00). The bottom panel illustrates the vertical formation sensitivity of O<sub>3</sub> corresponding to exceedance events. The squares and color bars are colored according to FNR<sub>sec</sub> threshold values determined from the GEOS-Chem model.**

455

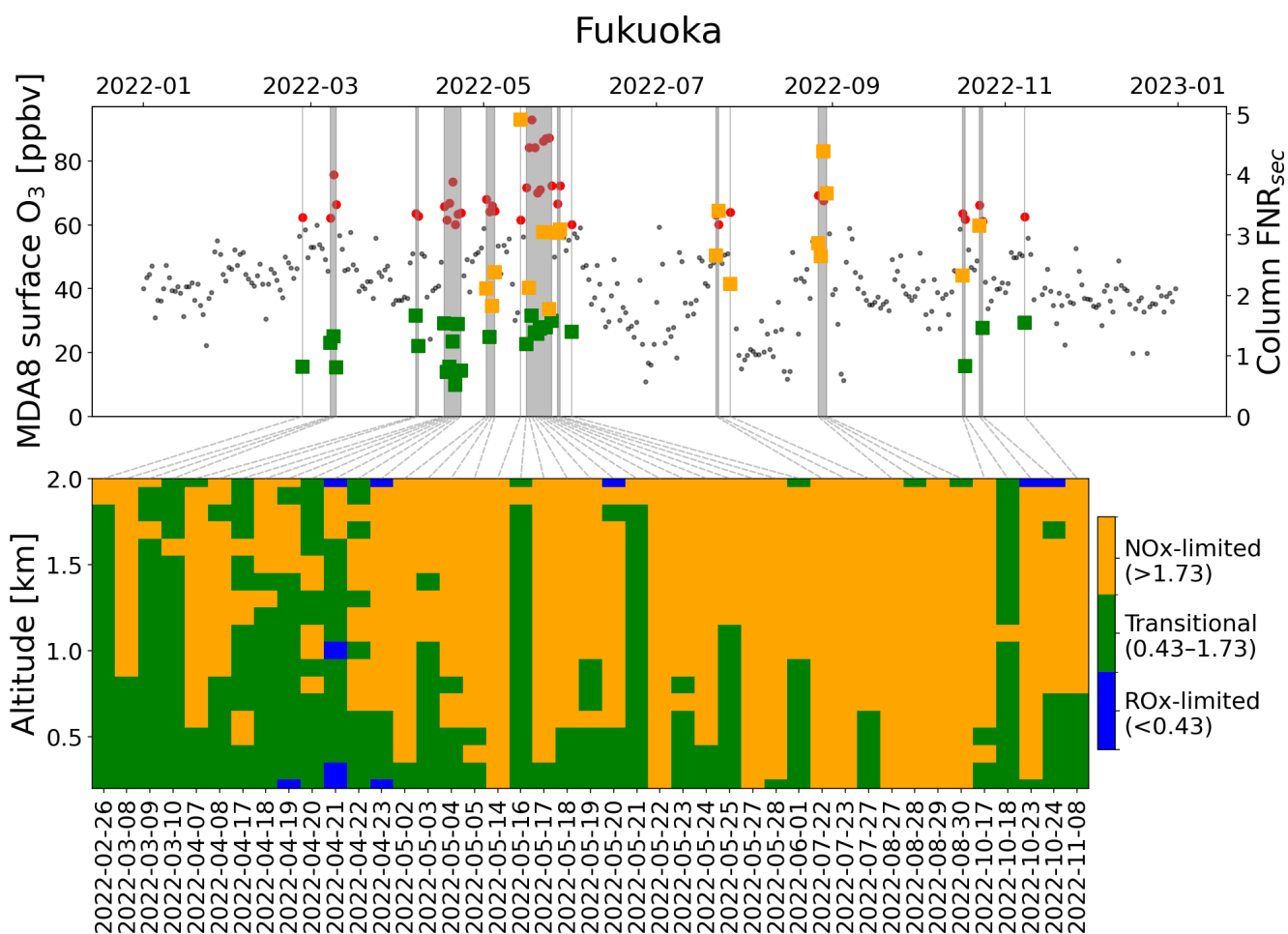


**Figure 11: Sensitivity analysis of O<sub>3</sub> during MDA8 exceedance events at Fukuoka. The top panel presents MDA8 surface O<sub>3</sub>, with non-exceedance days indicated by black dots and exceedance days shown as red points with grey shadows. Squares depict the column FNR<sub>sec</sub> derived from Pandora sky-scan measurements around local noon (12:00 ± 2:00). The bottom panel illustrates the vertical formation sensitivity of O<sub>3</sub> corresponding to exceedance events. The squares and color bars are colored according to FNR<sub>sec</sub> threshold values determined from the GEOS-Chem model.**

The exceedance events of O<sub>3</sub> spanned a broad period from spring through fall at both Tokyo-TMU and Fukuoka (Figs. 10 and 11). The column FNR<sub>sec</sub> were higher during summer leading to a dominant classification in the NO<sub>x</sub>-limited regime. Transitional conditions were observed more frequently during spring and fall. At Tokyo-TMU, only one exceedance event (7 April) was found to be sensitive to RO<sub>x</sub> radicals. The locally elevated NO<sub>x</sub> emissions on that event shifted the chemical environment downward to lower FNR<sub>sec</sub> values (Fig. S12). Vertical sensitivity profiles showed a RO<sub>x</sub>-limited regime within the lower 1 km on 7-8 April. For Fukuoka, the transitional condition occurred more frequently during the exceedance events, emphasizing the need for simultaneous control strategies targeting both NO<sub>x</sub> and VOCs in this region.

## 470 Conclusions

This study demonstrates the use of Pandora measurements to investigate O<sub>3</sub> sensitivity. Pandora provides vertical column densities and profiles of NO<sub>2</sub> and HCHO, which are valuable for a comprehensive understanding of O<sub>3</sub> production in the lower to mid-troposphere. Additionally, with the aid of the GEOS-Chem chemical transport model, we identified the region-specific thresholds to improve sensitivity analysis.

475 By applying the grid-stretching capability of the high-performance GEOS-Chem model, the diurnal cycles of NO<sub>2</sub>, HCHO, and O<sub>3</sub> were generally well reproduced. The correlation coefficients between the model and in situ surface measurements were 0.48 for NO<sub>2</sub> and 0.32 for HCHO, and from 0.53 to 0.61 for O<sub>3</sub>. For the tropospheric columns, the correlations between GEOS-Chem and Pandora ranged from 0.54 to 0.72 for NO<sub>2</sub>, and from 0.51 to 0.87 for HCHO.

According to the GEOS-Chem simulations, secondary HCHO was the dominant contributor to total HCHO, with its contribution increasing with altitude. Furthermore, the region-specific thresholds for the O<sub>3</sub> sensitivity regime were identified. The surface FNR<sub>sec</sub> values tended to be lower compared to the column FNR<sub>sec</sub>. The column FNR<sub>sec</sub> threshold ranges were 0.86–1.52 in Sapporo, 0.74–1.7 in Tsukuba-NIES, 0.62–1.53 in Tokyo-TMU, and 0.43–1.73 in Fukuoka.

Using the tropospheric column FNR<sub>sec</sub> during high O<sub>3</sub> episodes, the formation regime was found to be mainly NO<sub>x</sub>-limited during summer, due to increasing VOCs emissions and strong photochemical activity. The vertical distribution of O<sub>3</sub> sensitivity regimes was also obtained from the Pandora vertical profile. The diagnostics could assist regulators in reducing the frequency of O<sub>3</sub> exceedance events.

To mitigate O<sub>3</sub> exposure, particularly for sensitive groups, policymakers should prioritize VOC emission controls near the surface layers in higher-latitude locations. During summertime, greater attention should be paid to controlling local NO<sub>x</sub> emissions. Moreover, regional transport of NO<sub>x</sub> from large emission sources can contribute to elevated NO<sub>x</sub>, where the NO<sub>x</sub>-limited regime is dominant, thereby enhancing O<sub>3</sub> production.

### Data availability

The Pandora data are available at the PGN website (<https://www.pandonia-global-network.org>).

### Author contributions

NC: Conceptualization, Formal analysis, Writing (original draft preparation). HT: Conceptualization, Supervision, Writing (review and editing). SI: Conceptualization, Writing (review and editing). TF, MF, SK, and HT: Data curation, Writing (review and editing). KI, YD, AM and RU: Writing (review and editing).

### Competing interests

The authors declare that they have no conflict of interest.

### Acknowledgements

We thank the principal investigators, support staff, and funding for establishing and maintaining the Sapporo, Tsukuba-NIES, Tokyo-TMU, and Fukuoka sites of the PGN used in this investigation. The PGN is a bilateral project supported by funding from NASA and ESA. The model simulations were run using the NIES scalar processing supercomputer (HPE Apollo 2000). We thank Ms. Kimiko Suto (NIES) for managing the air monitoring data. This work was financially supported by JST SPRING, Grant Number JPMJSP2125. The author (N.D.T.C) would like to take this opportunity to thank the “THERS Make New Standards Program for the Next Generation Researchers”.

### References

- Abdi-Oskouei, M., Roozitalab, B., Stanier, C. O., Christiansen, M., Pfister, G., Pierce, R. B., McDonald, B. C., Adelman, Z., Janseen, M., Dickens, A. F., and Carmichael, G. R.: The Impact of Volatile Chemical Products, Other VOCs, and NO<sub>x</sub> on Peak Ozone in the Lake Michigan Region, *JGR Atmospheres*, 127, e2022JD037042, <https://doi.org/10.1029/2022JD037042>, 2022.
- Akimoto, H.: Overview of policy actions and observational data for PM<sub>2.5</sub> and O<sub>3</sub> in Japan: a study of urban air quality improvement in Asia, *JICA-RI Working Paper*, 137, 2017.

- Bates, K. H., Evans, M. J., Henderson, B. H., and Jacob, D. J.: Impacts of updated reaction kinetics on the global GEOS-Chem simulation of atmospheric chemistry, *Geosci. Model Dev.*, 17, 1511–1524, <https://doi.org/10.5194/gmd-17-1511-2024>, 2024.
- 515 Bindle, L., Martin, R. V., Cooper, M. J., Lundgren, E. W., Eastham, S. D., Auer, B. M., Clune, T. L., Weng, H., Lin, J., Murray, L. T., Meng, J., Keller, C. A., Putman, W. M., Pawson, S., and Jacob, D. J.: Grid-stretching capability for the GEOS-Chem 13.0.0 atmospheric chemistry model, *Geosci. Model Dev.*, 14, 5977–5997, <https://doi.org/10.5194/gmd-14-5977-2021>, 2021.
- Cede, A., Tiefengraber, M., Gebetsberger, M., and Kreuter, M.: Manual for Blick Software Suite 1.8, 2021a.
- 520 Cede, A., Tiefengraber, M., Gebetsberger, M., and Spinei, E.: Pandonia Global Network Data Products Readme Document, 2021b.
- Chang, L.-S., Ahn, S., Bae, M.-S., Park, S.-M., Gil, J., Kim, K.-R., Lee, G., Lee, T., Woo, J.-H., Park, R., Kwon, H.-A., Choo, G.-H., and Song, C.-K.: Role of factors controlling diurnal variation of cold-season formaldehyde during Satellite Integrated Joint Monitoring of Air Quality 2021 campaign, *Sci. Total Environ.*, 960, 178283, <https://doi.org/10.1016/j.scitotenv.2024.178283>, 2025.
- 525 Chatani, S., Kitayama, K., Itahashi, S., Irie, H., and Shimadera, H.: Effectiveness of emission controls implemented since 2000 on ambient ozone concentrations in multiple timescales in Japan: An emission inventory development and simulation study, *Sci. Total Environ.*, 894, 165058, <https://doi.org/10.1016/j.scitotenv.2023.165058>, 2023.
- Chen, Z., Sun, L., Huang, L., Xie, Y., Yang, S., Sun, L., Xue, J., and Yan, F.: Inequality of exposure to PM<sub>2.5</sub> and ozone among age groups and cities in Japan in 2030 and 2050, *Urban Clim.*, 55, 101935, <https://doi.org/10.1016/j.uclim.2024.101935>, 2024.
- 530 Choi, S., Lamsal, L. N., Follette-Cook, M., Joiner, J., Krotkov, N. A., Swartz, W. H., Pickering, K. E., Loughner, C. P., Appel, W., Pfister, G., Saide, P. E., Cohen, R. C., Weinheimer, A. J., and Herman, J. R.: Assessment of NO<sub>2</sub> observations during DISCOVER-AQ and KORUS-AQ field campaigns, *Atmos. Meas. Tech.*, 13, 2523–2546, <https://doi.org/10.5194/amt-13-2523-2020>, 2020.
- 535 Choo, G.-H., Lee, K., Hong, H., Jeong, U., Choi, W., and Janz, S. J.: Highly resolved mapping of NO<sub>2</sub> vertical column densities from GeoTASO measurements over a megacity and industrial area during the KORUS-AQ campaign, *Atmos. Meas. Tech.*, 16, 625–644, <https://doi.org/10.5194/amt-16-625-2023>, 2023.
- Douros, J., Eskes, H., Van Geffen, J., Boersma, K. F., Compernelle, S., Pinardi, G., Blechschmidt, A.-M., Peuch, V.-H., Colette, A., and Veeffkind, P.: Comparing Sentinel-5P TROPOMI NO<sub>2</sub> column observations with the CAMS regional air quality ensemble, *Geosci. Model Dev.*, 16, 509–534, <https://doi.org/10.5194/gmd-16-509-2023>, 2023.
- 540 Duncan, B. N., Yoshida, Y., Olson, J. R., Sillman, S., Martin, R. V., Lamsal, L., Hu, Y., Pickering, K. E., Retscher, C., Allen, D. J., and Crawford, J. H.: Application of OMI observations to a space-based indicator of NO<sub>x</sub> and VOC controls on surface ozone formation, *Atmos. Environ.*, 44, 2213–2223, <https://doi.org/10.1016/j.atmosenv.2010.03.010>, 2010.
- Eastham, S. D., Long, M. S., Keller, C. A., Lundgren, E., Yantosca, R. M., Zhuang, J., Li, C., Lee, C. J., Yannetti, M., Auer, B. M., Clune, T. L., Kouatchou, J., Putman, W. M., Thompson, M. A., Trayanov, A. L., Molod, A. M., Martin, R. V., and Jacob, D. J.: GEOS-Chem High Performance (GCHP v11-02c): a next-generation implementation of the GEOS-Chem chemical transport model for massively parallel applications, *Geosci. Model Dev.*, 11, 2941–2953, <https://doi.org/10.5194/gmd-11-2941-2018>, 2018.
- 545 Feng, Z., Agathokleous, E., Yue, X., Oksanen, E., Paoletti, E., Sase, H., Gandin, A., Koike, T., Calatayud, V., Yuan, X., Liu, X., De Marco, A., Jolivet, Y., Kontunen-Soppela, S., Hoshika, Y., Saji, H., Li, P., Li, Z., Watanabe, M., et al.: Emerging challenges of ozone impacts on asian plants: actions are needed to protect ecosystem health, *Ecosyst Health Sustain*, 7, 1911602, <https://doi.org/10.1080/20964129.2021.1911602>, 2021.
- Grulke, N. E. and Heath, R. L.: Ozone effects on plants in natural ecosystems, *Plant Biol J*, 22, 12–37, <https://doi.org/10.1111/plb.12971>, 2020.
- 555 Hammer, M. -U., Vogel, B., and Vogel, H.: Findings on H<sub>2</sub> O<sub>2</sub> /HNO<sub>3</sub> as an indicator of ozone sensitivity in Baden-Württemberg, Berlin-Brandenburg, and the Po valley based on numerical simulations, *J.-Geophys.-Res.*, 107, <https://doi.org/10.1029/2000JD000211>, 2002.
- 560 Herman, J. and Mao, J.: Seasonal Variation of Total Column Formaldehyde, Nitrogen Dioxide, and Ozone Over Various Pandora Spectrometer Sites with a Comparison of OMI and Diurnally Varying DSCOVR-EPIC Satellite Data, <https://doi.org/10.5194/egusphere-2024-1216>, 6 May 2024.

- Herman, J., Cede, A., Spinei, E., Mount, G., Tzortziou, M., and Abuhassan, N.: NO<sub>2</sub> column amounts from ground-based Pandora and MFDOAS spectrometers using the direct-sun DOAS technique: Intercomparisons and application to OMI validation, *J. Geophys. Res. Atmos.*, 114, 2009JD011848, <https://doi.org/10.1029/2009JD011848>, 2009.
- 565 Hong, Q., Zhu, L., Xing, C., Hu, Q., Lin, H., Zhang, C., Zhao, C., Liu, T., Su, W., and Liu, C.: Inferring vertical variability and diurnal evolution of O<sub>3</sub> formation sensitivity based on the vertical distribution of summertime HCHO and NO<sub>2</sub> in Guangzhou, China, *Sci. Total Environ.*, 827, 154045, <https://doi.org/10.1016/j.scitotenv.2022.154045>, 2022.
- Hu, Q., Ji, X., Hong, Q., Li, J., Li, Q., Ou, J., Liu, H., Xing, C., Tan, W., Chen, J., Chang, B., and Liu, C.: Vertical Evolution of Ozone Formation Sensitivity Based on Synchronous Vertical Observations of Ozone and Proxies for Its Precursors: Implications for Ozone Pollution Prevention Strategies, *Environ. Sci. Technol.*, *acs.est.4c00637*, <https://doi.org/10.1021/acs.est.4c00637>, 2024.
- 570 Inoue, K., Tonokura, K., and Yamada, H.: Modeling study on the spatial variation of the sensitivity of photochemical ozone concentrations and population exposure to VOC emission reductions in Japan, *Air Qual. Atmos. Health.*, 12, 1035–1047, <https://doi.org/10.1007/s11869-019-00720-w>, 2019.
- Irie, H., Takashima, H., Kanaya, Y., Boersma, K. F., Gast, L., Wittrock, F., Brunner, D., Zhou, Y., and Van Roozendael, M.: Eight-component retrievals from ground-based MAX-DOAS observations, *Atmos. Meas. Tech.*, 4, 1027–1044, <https://doi.org/10.5194/amt-4-1027-2011>, 2011.
- Irie, H., Yonekawa, D., Damiani, A., Hoque, H. M. S., Sudo, K., and Itahashi, S.: Continuous multi-component MAX-DOAS observations for the planetary boundary layer ozone variation analysis at Chiba and Tsukuba, Japan, from 2013 to 2019, *Prog. Earth Planet. Sci.*, 8, 31, <https://doi.org/10.1186/s40645-021-00424-9>, 2021.
- 580 Itahashi, S. and Irie, H.: Surface and aloft NO<sub>2</sub> pollution over the greater Tokyo area observed by ground-based and MAX-DOAS measurements bridged by kilometer-scale regional air quality modeling, *Prog. Earth Planet. Sci.*, 9, 15, <https://doi.org/10.1186/s40645-022-00474-7>, 2022.
- Jin, X., Fiore, A. M., Murray, L. T., Valin, L. C., Lamsal, L. N., Duncan, B., Folkert Boersma, K., De Smedt, I., Abad, G. G., Chance, K., and Tonnesen, G. S.: Evaluating a Space-Based Indicator of Surface Ozone-NO<sub>x</sub>-VOC Sensitivity Over Midlatitude Source Regions and Application to Decadal Trends, *JGR Atmospheres*, 122, <https://doi.org/10.1002/2017JD026720>, 2017.
- 585 Judd, L. M., Al-Saadi, J. A., Janz, S. J., Kowalewski, M. G., Pierce, R. B., Szykman, J. J., Valin, L. C., Swap, R., Cede, A., Mueller, M., Tiefengraber, M., Abuhassan, N., and Williams, D.: Evaluating the impact of spatial resolution on tropospheric NO<sub>2</sub> column comparisons within urban areas using high-resolution airborne data, *Atmos. Meas. Tech.*, 12, 6091–6111, <https://doi.org/10.5194/amt-12-6091-2019>, 2019.
- 590 Judd, L. M., Al-Saadi, J. A., Szykman, J. J., Valin, L. C., Janz, S. J., Kowalewski, M. G., Eskes, H. J., Veeffkind, J. P., Cede, A., Mueller, M., Gebetsberger, M., Swap, R., Pierce, R. B., Nowlan, C. R., Abad, G. G., Nehrir, A., and Williams, D.: Evaluating Sentinel-5P TROPOMI tropospheric NO<sub>2</sub> column densities with airborne and Pandora spectrometers near New York City and Long Island Sound, *Atmos. Meas. Tech.*, 13, 6113–6140, <https://doi.org/10.5194/amt-13-6113-2020>, 2020.
- 595 Jung, J., Choi, Y., Mousavinezhad, S., Kang, D., Park, J., Pouyaei, A., Ghahremanloo, M., Momeni, M., and Kim, H.: Changes in the ozone chemical regime over the contiguous United States inferred by the inversion of NO<sub>x</sub> and VOC emissions using satellite observation, *Atmos. Res.*, 270, 106076, <https://doi.org/10.1016/j.atmosres.2022.106076>, 2022.
- Kim, S., Kim, D., Hong, H., Chang, L.-S., Lee, H., Kim, D.-R., Kim, D., Yu, J.-A., Lee, D., Jeong, U., Song, C.-K., Kim, S.-W., Park, S. S., Kim, J., Hanisco, T. F., Park, J., Choi, W., and Lee, K.: First-time comparison between NO<sub>2</sub> vertical columns from Geostationary Environmental Monitoring Spectrometer (GEMS) and Pandora measurements, *Atmos. Meas. Tech.*, 16, 3959–3972, <https://doi.org/10.5194/amt-16-3959-2023>, 2023.
- 600 Kleinman, L. I., Daum, P. H., Lee, Y., Nunnermacker, L. J., Springston, S. R., Weinstein-Lloyd, J., and Rudolph, J.: Sensitivity of ozone production rate to ozone precursors, *Geophysical Research Letters*, 28, 2903–2906, <https://doi.org/10.1029/2000GL012597>, 2001.
- 605 Kurokawa, J. and Ohara, T.: Long-term historical trends in air pollutant emissions in Asia: Regional Emission inventory in ASia (REAS) version 3, *Atmos. Chem. Phys.*, 20, 12761–12793, <https://doi.org/10.5194/acp-20-12761-2020>, 2020.
- Langford, V. S., Dryahina, K., and Španěl, P.: Robust Automated SIFT-MS Quantitation of Volatile Compounds in Air Using a Multicomponent Gas Standard, *J. Am. Soc. Mass Spectrom.*, 34, 2630–2645, <https://doi.org/10.1021/jasms.3c00312>, 2023.

- 610 Lin, H., Jacob, D. J., Lundgren, E. W., Sulprizio, M. P., Keller, C. A., Fritz, T. M., Eastham, S. D., Emmons, L. K., Campbell, P. C., Baker, B., Saylor, R. D., and Montuoro, R.: Harmonized Emissions Component (HEMCO) 3.0 as a versatile emissions component for atmospheric models: application in the GEOS-Chem, NASA GEOS, WRF-GC, CESM2, NOAA GEFS-Aerosol, and NOAA UFS models, *Geosci. Model Dev.*, 14, 5487–5506, <https://doi.org/10.5194/gmd-14-5487-2021>, 2021.
- 615 Lin, H., Xing, C., Hong, Q., Liu, C., Ji, X., Liu, T., Lin, J., Lu, C., Tan, W., Li, Q., and Liu, H.: Diagnosis of Ozone Formation Sensitivities in Different Height Layers via MAX-DOAS Observations in Guangzhou, *JGR Atmospheres*, 127, e2022JD036803, <https://doi.org/10.1029/2022JD036803>, 2022.
- Liu, H., Liu, S., Xue, B., Lv, Z., Meng, Z., Yang, X., Xue, T., Yu, Q., and He, K.: Ground-level ozone pollution and its health impacts in China, *Atmos. Environ.*, 173, 223–230, <https://doi.org/10.1016/j.atmosenv.2017.11.014>, 2018.
- 620 Liu, O., Li, Z., Lin, Y., Fan, C., Zhang, Y., Li, K., Zhang, P., Wei, Y., Chen, T., Dong, J., and De Leeuw, G.: Evaluation of the first year of Pandora NO<sub>2</sub> measurements over Beijing and application to satellite validation, *Atmos. Meas. Tech.*, 17, 377–395, <https://doi.org/10.5194/amt-17-377-2024>, 2024.
- Mahmood, F., Khokhar, M. F., and Mahmood, Z.: Examining the relationship of tropospheric ozone and climate change on crop productivity using the multivariate panel data techniques, *J. Environ. Manag.*, 272, 111024, <https://doi.org/10.1016/j.jenvman.2020.111024>, 2020.
- 625 Martin, R. V., Eastham, S. D., Bindle, L., Lundgren, E. W., Clune, T. L., Keller, C. A., Downs, W., Zhang, D., Lucchesi, R. A., Sulprizio, M. P., Yantosca, R. M., Li, Y., Estrada, L., Putman, W. M., Auer, B. M., Trayanov, A. L., Pawson, S., and Jacob, D. J.: Improved Advection, Resolution, Performance, and Community Access in the New Generation (Version 13) of the High Performance GEOS-Chem Global Atmospheric Chemistry Model (GCHP), <https://doi.org/10.5194/gmd-2022-42>, 24 February 2022.
- 630 McDuffie, E., Smith, S., O'Rourke, P., Tibrewal, K., Venkataraman, C., Marais, E., Zheng, B., Crippa, M., Brauer, M., and Martin, R.: CEDS\_GBD-MAPS: Global Anthropogenic Emission Inventory of NO<sub>x</sub>, SO<sub>2</sub>, CO, NH<sub>3</sub>, NMVOCs, BC, and OC from 1970-2017 (2020\_v1.0), <https://doi.org/10.5281/ZENODO.3754964>, 2020.
- McLinden, C. A., Olsen, S. C., Hannegan, B., Wild, O., Prather, M. J., and Sundet, J.: Stratospheric ozone in 3-D models: A simple chemistry and the cross-tropopause flux, *J. Geophys. Res. Atmos.*, 105, 14653–14665, <https://doi.org/10.1029/2000JD900124>, 2000.
- 635 Mishra, M., Chen, P.-H., Lin, G.-Y., Nguyen, T.-T.-N., Le, T.-C., Dejchanchaiwong, R., Tekasakul, P., Shih, S.-H., Jhang, C.-W., and Tsai, C.-J.: Photochemical oxidation of VOCs and their source impact assessment on ozone under de-weather conditions in Western Taiwan, *Environ. Pollut.*, 346, 123662, <https://doi.org/10.1016/j.envpol.2024.123662>, 2024.
- Mouat, A. P., Spinei, E., and Kaiser, J.: Informing Near-Airport Satellite NO<sub>2</sub> Retrievals Using Pandora Sky-Scanning Observations, *ACS EST Air*, 1, 1617–1628, <https://doi.org/10.1021/acsestair.4c00158>, 2024.
- 640 Nuvolone, D., Petri, D., and Voller, F.: The effects of ozone on human health, *Environ. Sci. Pollut. Res.*, 25, 8074–8088, <https://doi.org/10.1007/s11356-017-9239-3>, 2018.
- Prather, M. J.: Photolysis rates in correlated overlapping cloud fields: Cloud-J 7.3c, *Geosci. Model Dev.*, 8, 2587–2595, <https://doi.org/10.5194/gmd-8-2587-2015>, 2015.
- 645 Qian, Y., Wang, D., Li, Z., Liu, H., Zhou, H., Dou, K., Xi, L., Tang, F., Si, F., and Luo, Y.: Ground-based MAX-DOAS observations of tropospheric formaldehyde and nitrogen dioxide: Insights into ozone formation sensitivity, *Atmos. Pollut. Res.*, 15, 102285, <https://doi.org/10.1016/j.apr.2024.102285>, 2024.
- Ramya, A., Dhevagi, P., Poornima, R., Avudainayagam, S., Watanabe, M., and Agathokleous, E.: Effect of ozone stress on crop productivity: A threat to food security, *Environ. Res.*, 236, 116816, <https://doi.org/10.1016/j.envres.2023.116816>, 2023.
- 650 Rawat, P., Crawford, J. H., Travis, K. R., Judd, L. M., Demetillo, M. A. G., Valin, L. C., Szykman, J. J., Whitehill, A., Baumann, E., and Hanisco, T. F.: Maximizing the scientific application of Pandora column observations of HCHO and NO<sub>2</sub>, *Atmos. Meas. Tech.*, 18, 2899–2917, <https://doi.org/10.5194/amt-18-2899-2025>, 2025.
- Roberts, I. J., Carpenter, L. J., Shaw, M. D., and Langford, V. S.: Selected Ion Flow Tube – Mass Spectrometry (SIFT-MS) study of the reactions of H<sub>3</sub>O<sup>+</sup>, NO<sup>+</sup> and O<sub>2</sub><sup>+</sup> with a range of oxygenated volatile organic carbons (OVOCs), *Int. J. Mass Spectrom.*, 479, 116892, <https://doi.org/10.1016/j.ijms.2022.116892>, 2022.

- 655 Ryan, R. G., Marais, E. A., Gershenson-Smith, E., Ramsay, R., Muller, J.-P., Tirpitz, J.-L., and Frieß, U.: Measurement report: MAX-DOAS measurements characterise Central London ozone pollution episodes during 2022 heatwaves, *Atmos. Chem. Phys.*, 23, 7121–7139, <https://doi.org/10.5194/acp-23-7121-2023>, 2023.
- Sadanaga, Y., Kawasaki, S., Tanaka, Y., Kajii, Y., and Bandow, H.: New System for Measuring the Photochemical Ozone Production Rate in the Atmosphere, *Environ. Sci. Technol.*, 51, 2871–2878, <https://doi.org/10.1021/acs.est.6b04639>, 2017.
- 660 Sakamoto, Y., Sadanaga, Y., Li, J., Matsuoka, K., Takemura, M., Fujii, T., Nakagawa, M., Kohno, N., Nakashima, Y., Sato, K., Nakayama, T., Kato, S., Takami, A., Yoshino, A., Murano, K., and Kajii, Y.: Relative and Absolute Sensitivity Analysis on Ozone Production in Tsukuba, a City in Japan, *Environ. Sci. Technol.*, 53, 13629–13635, <https://doi.org/10.1021/acs.est.9b03542>, 2019.
- Santiago, J. V., Inoue, K., and Tonokura, K.: Diagnosis of ozone formation sensitivity in the Mexico City Metropolitan Area using HCHO/NO<sub>2</sub> column ratios from the ozone monitoring instrument, *Environ. Adv.*, 6, 100138, <https://doi.org/10.1016/j.envadv.2021.100138>, 2021.
- Schroeder, J. R., Crawford, J. H., Fried, A., Walega, J., Weinheimer, A., Wisthaler, A., Müller, M., Mikoviny, T., Chen, G., Shook, M., Blake, D. R., and Tonnesen, G. S.: New insights into the column CH<sub>2</sub>O/NO<sub>2</sub> ratio as an indicator of near-surface ozone sensitivity, *JGR Atmospheres*, 122, 8885–8907, <https://doi.org/10.1002/2017JD026781>, 2017.
- 670 Shi, Y., Wang, S., Zhang, S., Liu, J., Jin, D., Huo, J., Xue, R., Zhu, J., Gu, C., and Zhou, B.: HCHO and NO<sub>2</sub> profile characteristics under different synoptic patterns in Shanghai, China, *J. Environ. Sci.*, S1001074225000427, <https://doi.org/10.1016/j.jes.2025.01.028>, 2025a.
- Shi, Y., Wang, S., Zhang, S., Liu, J., Jin, D., Huo, J., Xue, R., Zhu, J., Gu, C., and Zhou, B.: HCHO and NO<sub>2</sub> profile characteristics under different synoptic patterns in Shanghai, China, *J. Environ. Sci.*, S1001074225000427, 675 <https://doi.org/10.1016/j.jes.2025.01.028>, 2025b.
- Sillman, S. and He, D.: Some theoretical results concerning O<sub>3</sub>-NO<sub>x</sub>-VOC chemistry and NO<sub>x</sub>-VOC indicators, *J.-Geophys.-Res.*, 107, <https://doi.org/10.1029/2001JD001123>, 2002.
- Souri, A. H., Chance, K., Bak, J., Nowlan, C. R., González Abad, G., Jung, Y., Wong, D. C., Mao, J., and Liu, X.: Unraveling pathways of elevated ozone induced by the 2020 lockdown in Europe by an observationally constrained regional model using TROPOMI, *Atmos. Chem. Phys.*, 21, 18227–18245, <https://doi.org/10.5194/acp-21-18227-2021>, 2021.
- Souri, A. H., Johnson, M. S., Wolfe, G. M., Crawford, J. H., Fried, A., Wisthaler, A., Brune, W. H., Blake, D. R., Weinheimer, A. J., Verhoelst, T., Compernelle, S., Pinardi, G., Vigouroux, C., Langerock, B., Choi, S., Lamsal, L., Zhu, L., Sun, S., Cohen, R. C., et al.: Characterization of errors in satellite-based HCHO/NO<sub>2</sub> tropospheric column ratios with respect to chemistry, column-to-PBL translation, spatial representation, and retrieval uncertainties, *Atmos. Chem. Phys.*, 23, 1963–1986, 685 <https://doi.org/10.5194/acp-23-1963-2023>, 2023a.
- Souri, A. H., Kumar, R., Chong, H., Golbazi, M., Knowland, K. E., Geddes, J., and Johnson, M. S.: Decoupling in the vertical shape of HCHO during a sea breeze event: The effect on trace gas satellite retrievals and column-to-surface translation, *Atmos. Environ.*, 309, 119929, <https://doi.org/10.1016/j.atmosenv.2023.119929>, 2023b.
- Souri, A. H., Kumar, R., Chong, H., Golbazi, M., Knowland, K. E., Geddes, J., and Johnson, M. S.: Decoupling in the vertical shape of HCHO during a sea breeze event: The effect on trace gas satellite retrievals and column-to-surface translation, *Atmospheric Environment*, 309, 119929, <https://doi.org/10.1016/j.atmosenv.2023.119929>, 2023c.
- Souri, A. H., González Abad, G., Wolfe, G. M., Verhoelst, T., Vigouroux, C., Pinardi, G., Compernelle, S., Langerock, B., Duncan, B. N., and Johnson, M. S.: Feasibility of robust estimates of ozone production rates using a synergy of satellite observations, ground-based remote sensing, and models, *Atmos. Chem. Phys.*, 25, 2061–2086, <https://doi.org/10.5194/acp-25-2061-2025>, 2025. 695
- Spinei, E., Whitehill, A., Fried, A., Tiefengraber, M., Knepp, T. N., Herndon, S., Herman, J. R., Müller, M., Abuhassan, N., Cede, A., Richter, D., Walega, J., Crawford, J., Szykman, J., Valin, L., Williams, D. J., Long, R., Swap, R. J., Lee, Y., et al.: The first evaluation of formaldehyde column observations by improved Pandora spectrometers during the KORUS-AQ field study, *Atmos. Meas. Tech.*, 11, 4943–4961, <https://doi.org/10.5194/amt-11-4943-2018>, 2018.
- 700 Su, W., Liu, C., Hu, Q., Zhao, S., Sun, Y., Wang, W., Zhu, Y., Liu, J., and Kim, J.: Primary and secondary sources of ambient formaldehyde in the Yangtze River Delta based on Ozone Mapping and Profiler Suite (OMPS) observations, *Atmos. Chem. Phys.*, 19, 6717–6736, <https://doi.org/10.5194/acp-19-6717-2019>, 2019.

- 705 Thorp, T., Arnold, S. R., Pope, R. J., Spracklen, D. V., Conibear, L., Knote, C., Arshinov, M., Belan, B., Asmi, E., Laurila, T., Skorokhod, A. I., Nieminen, T., and Petäjä, T.: Late-spring and summertime tropospheric ozone and NO<sub>2</sub> in western Siberia and the Russian Arctic: regional model evaluation and sensitivities, *Atmos. Chem. Phys.*, 21, 4677–4697, <https://doi.org/10.5194/acp-21-4677-2021>, 2021.
- 710 Tirpitz, J.-L., Frieß, U., Hendrick, F., Alberti, C., Allaart, M., Apituley, A., Bais, A., Beirle, S., Berkhout, S., Bogner, K., Bösch, T., Bruchkouski, I., Cede, A., Chan, K. L., Den Hoed, M., Donner, S., Drosoglou, T., Fayt, C., Friedrich, M. M., et al.: Intercomparison of MAX-DOAS vertical profile retrieval algorithms: studies on field data from the CINDI-2 campaign, *Atmos. Meas. Tech.*, 14, 1–35, <https://doi.org/10.5194/amt-14-1-2021>, 2021.
- 715 Tonnesen, G. S. and Dennis, R. L.: Analysis of radical propagation efficiency to assess ozone sensitivity to hydrocarbons and NO<sub>x</sub>: 2. Long-lived species as indicators of ozone concentration sensitivity, *J. Geophys. Res. Atmos.*, 105, 9227–9241, <https://doi.org/10.1029/1999jd900372>, 2000.
- Travis, K. R. and Jacob, D. J.: Systematic bias in evaluating chemical transport models with maximum daily 8 h average (MDA8) surface ozone for air quality applications: a case study with GEOS-Chem v9.02, *Geosci. Model Dev.*, 12, 3641–3648, <https://doi.org/10.5194/gmd-12-3641-2019>, 2019.
- 720 Travis, K. R., Jacob, D. J., Fisher, J. A., Kim, P. S., Marais, E. A., Zhu, L., Yu, K., Miller, C. C., Yantosca, R. M., Sulprizio, M. P., Thompson, A. M., Wennberg, P. O., Crounse, J. D., St. Clair, J. M., Cohen, R. C., Laughner, J. L., Dibb, J. E., Hall, S. R., Ullmann, K., et al.: Why do models overestimate surface ozone in the Southeast United States?, *Atmos. Chem. Phys.*, 16, 13561–13577, <https://doi.org/10.5194/acp-16-13561-2016>, 2016.
- 725 Van Der Werf, G. R., Randerson, J. T., Giglio, L., Van Leeuwen, T. T., Chen, Y., Rogers, B. M., Mu, M., Van Marle, M. J. E., Morton, D. C., Collatz, G. J., Yokelson, R. J., and Kasibhatla, P. S.: Global fire emissions estimates during 1997–2016, *Earth Syst. Sci. Data*, 9, 697–720, <https://doi.org/10.5194/essd-9-697-2017>, 2017.
- 730 Verhoelst, T., Compornelle, S., Pinardi, G., Lambert, J.-C., Eskes, H. J., Eichmann, K.-U., Fjærraa, A. M., Granville, J., Niemeijer, S., Cede, A., Tiefengraber, M., Hendrick, F., Pazmiño, A., Bais, A., Bazureau, A., Boersma, K. F., Bogner, K., Dehn, A., Donner, S., et al.: Ground-based validation of the Copernicus Sentinel-5P TROPOMI NO<sub>2</sub> measurements with the NDACC ZSL-DOAS, MAX-DOAS and Pandonia global networks, *Atmos. Meas. Tech.*, 14, 481–510, <https://doi.org/10.5194/amt-14-481-2021>, 2021.
- Wang, H., Welch, A. M., Nagalingam, S., Leong, C., Czimczik, C. I., Tang, J., Seco, R., Rinnan, R., Vettikkat, L., Schobesberger, S., Holst, T., Brijesh, S., Sheesley, R. J., Barsanti, K. C., and Guenther, A. B.: High temperature sensitivity of Arctic isoprene emissions explained by sedges, *Nat. Commun.*, 15, 6144, <https://doi.org/10.1038/s41467-024-49960-0>, 2024.
- 735 Wang, Z., Zhang, H., Shi, C., Ji, X., Zhu, Y., Xia, C., Sun, X., Zhang, M., Lin, X., Yan, S., Zhou, Y., Xing, C., Chen, Y., and Liu, C.: Vertical and spatial differences in ozone formation sensitivities under different ozone pollution levels in eastern Chinese cities, *npj Clim Atmos Sci*, 8, 30, <https://doi.org/10.1038/s41612-024-00855-3>, 2025.
- Weng, H., Lin, J., Martin, R., Millet, D. B., Jaeglé, L., Ridley, D., Keller, C., Li, C., Du, M., and Meng, J.: Global high-resolution emissions of soil NO<sub>x</sub>, sea salt aerosols, and biogenic volatile organic compounds, *Sci Data*, 7, 148, <https://doi.org/10.1038/s41597-020-0488-5>, 2020.
- 740 Wu, W., Fu, T.-M., Arnold, S. R., Spracklen, D. V., Zhang, A., Tao, W., Wang, X., Hou, Y., Mo, J., Chen, J., Li, Y., Feng, X., Lin, H., Huang, Z., Zheng, J., Shen, H., Zhu, L., Wang, C., Ye, J., et al.: Temperature-Dependent Evaporative Anthropogenic VOC Emissions Significantly Exacerbate Regional Ozone Pollution, *Environ. Sci. Technol.*, 58, 5430–5441, <https://doi.org/10.1021/acs.est.3c09122>, 2024.
- 745 Xing, C., Liu, C., Hong, Q., Liu, H., Wu, H., Lin, J., Song, Y., Chen, Y., Liu, T., Hu, Q., Tan, W., and Lin, H.: Vertical distributions and potential sources of wintertime atmospheric pollutants and the corresponding ozone production on the coast of Bohai Sea, *J. Environ. Manage.*, 319, 115721, <https://doi.org/10.1016/j.jenvman.2022.115721>, 2022.
- Xu, X., Huang, L., Yao, L., Yoshida, Y., and Long, Y.: Rising socio-economic costs of PM<sub>2.5</sub> pollution and medical service mismatching, *Nat Sustain*, 8, 265–275, <https://doi.org/10.1038/s41893-025-01509-9>, 2025.
- 750 Xue, J., Zhao, T., Luo, Y., Miao, C., Su, P., Liu, F., Zhang, G., Qin, S., Song, Y., Bu, N., and Xing, C.: Identification of ozone sensitivity for NO<sub>2</sub> and secondary HCHO based on MAX-DOAS measurements in northeast China, *Environ. Int.*, 160, 107048, <https://doi.org/10.1016/j.envint.2021.107048>, 2022.

Zhang, S., Wang, S., Zhang, R., Guo, Y., Yan, Y., Ding, Z., and Zhou, B.: Investigating the Sources of Formaldehyde and Corresponding Photochemical Indications at a Suburb Site in Shanghai From MAX-DOAS Measurements, *J. Geophys. Res. Atmos.*, 126, e2020JD033351, <https://doi.org/10.1029/2020JD033351>, 2021.

755 Zogka, A. G., Romanias, M. N., and Thevenet, F.: Formaldehyde and glyoxal measurement deploying a selected ion flow tube mass spectrometer (SIFT-MS), *Atmos. Meas. Tech.*, 15, 2001–2019, <https://doi.org/10.5194/amt-15-2001-2022>, 2022.